CFD Benchmark Tests for Indoor Environmental Problems: Part 2 Cross-Ventilation Airflows and Floor Heating Systems

Kazuhide Ito*, Kiao Inthavong, Takashi Kurabuchi, Toshikatsu Ueda, Tomoyuki Endo, Toshiaki Omori, Hiroki Ono, Shinsuke Kato, Koji Sakai, Yoshihide Suwa, Hiroshi Matsumoto, Hajime Yoshino, Weirong Zhang and Jiyuan Tu

Interdisciplinary Graduate School of Engineering Science, Kyushu University, 6-1 Kasuga-koen, Kasuga, Fukuoka, 816-8580 Japan

Abstract: Commercial Computational Fluid Dynamics (CFD) software is practically applied in indoor environmental design recent years but the prediction accuracy of CFD simulation depends on the understanding for the fundamentals of fluid dynamics and the setting of appropriate boundary and numerical conditions as well. Additionally, deeper understanding to a specific problem regarding indoor environment is also requested. The series of this study aimed to provide with the practical information such as prediction accuracy and problematic areas related to CFD applications in indoor environment, air conditioning and ventilation, then performed benchmark tests and reported the results. In this Part 2, benchmark test results for cross-ventilation airflows and floor heating systems were introduced.

The highest reproducibility of the predicted results compared with the wind tunnel results occurred when the Z_0-type wall function was used as the floor-surface boundary condition and the SST k–ω for the turbulence model in case of cross-ventilation flow and SST k–ω model showed also the closest matching results with experiment in case of natural convection in a room with floor heating.

Keywords: Indoor environment, Computational Fluid Dynamics, Benchmark test, Cross-ventilation airflows, floor heating systems.

1. INTRODUCTION

The overarching objective of this study is to compile benchmark test results of CFD that relate to indoor environmental problem. Though various types of flow fields are found in indoor environment, we have classified those flow fields into eight categories based on literature review: (1) Isothermal 2-D/3-D airflows, (2) Non-isothermal 2-D/3-D airflows, (3) Cross-ventilation airflows, (4) Floor heating (panel) systems, (5) Numerical thermal manikins, (6) Air-conditioning airflows, (7) Residential kitchen airflows, (8) Fire-induced flow. Concerning the benchmark test results for targeting (1) Isothermal 2-D/3-D airflows and (2) Non-isothermal 2-D/3-D airflows, the details have been discussed in previous reported paper of this research series (Part 1 Benchmark test for isothermal/non-isothermal flow in 2D and 3D room model [1]). In this paper, benchmark test results for (3) Cross-ventilation airflows, (4) Floor heating (panel) systems, were introduced and discussed.

2. BENCHMARK TEST FOR CROSS-VENTILATION AIRFLOW

The need for energy efficient buildings such as eco-friendly offices and passive houses have seen CFD analysis become increasingly adopted to predict airflows in a room generated by natural ventilation, especially at the design stage of actual building construction. CFD results of ventilation airflows depend on factors such as grid type, differencing scheme, and turbulence model; therefore, typically, empirical rules are used as the basis for fully considering these factors for optimal choice. An inaccurate CFD analysis may affect the results of ventilation network design, which uses the CFD results such as pressure coefficients as its initial boundary conditions. Here, benchmark test for cross-ventilation airflow are taken in account and we discuss how ventilation airflows in a room and airflows around a building predicted by the CFD analyses are affected by varying boundary and numerical conditions.

2.1. Outline of Calculations

Figure **1** shows the external surrounding area around the target building, and Figure **2** shows the model of the target building. The discretized area was X: Y: Z = 58: 48: 60. The building has a simple geometry with the dimensions, width: depth: height ratio of 2 : 2 : 1, and a horizontal opening of 0.2 × 0.4 (dimensionless) in the center of two walls facing each other. Code G [Open FOAM, see Note at the end of paper] was used for the commercial CFD software. The wind tunnel experimental results are presented in Figures **3-7** based on the authors previous work described in [2-5]. The inlet conditions were based on the airflow distribution obtained from the wind tunnel

*Address correspondence to this author at the Interdisciplinary Graduate School of Engineering Science, Kyushu University, 6-1 Kasuga-koen, Kasuga, Fukuoka, 816-8580 Japan; Tel: +81 92 583 7628; Fax: +81 92 583 7627; Email: ito@kyudai.jp

E-ISSN: 2409-9821/15

experiment, and the angle of wind direction was set to 0° and 45°. Inflow conditions for the airflow-around-building differed from those for the ventilation airflow analysis. Generalized log-law type wall function, and Z_0-type wall function were used for the boundary conditions of the floor-surface of the analysis area. Four turbulence models were evaluated: the standard k–ε model, RNG k–ε model, realizable k–ε model, and the SST k–ω model. Other boundary conditions are given in Table **1**.

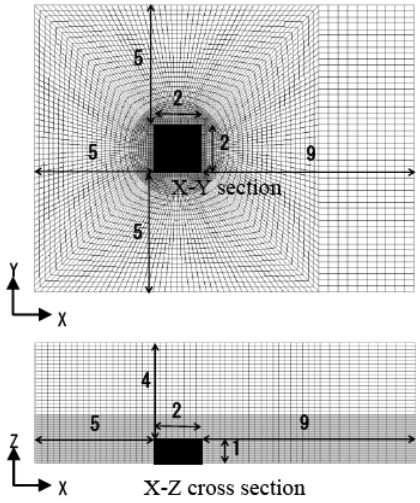

Figure 1: Computational domain of the external analysis area.

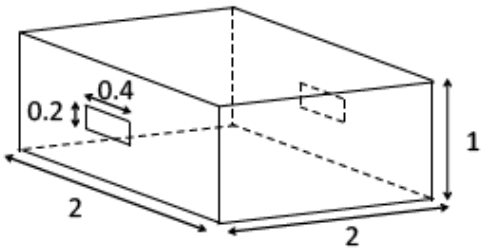

Figure 2: Building model to be analyzed.

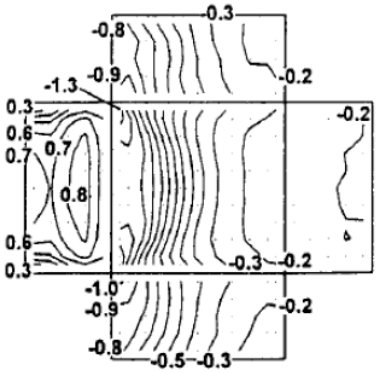

Figure 3: Wind tunnel experimental results showing wind pressure coefficient distribution for wind direction angle of 0° [4, 5].

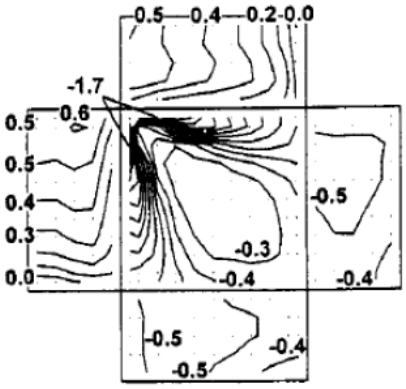

Figure 4: Wind tunnel experimental results showing wind pressure coefficient distribution for wind direction angle of 45° [4,5].

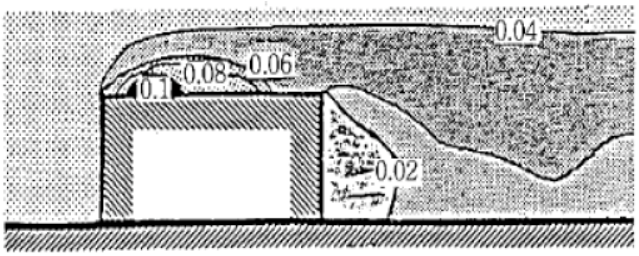

Figure 5: Distribution of turbulence kinetic energy from wind tunnel [4,5].

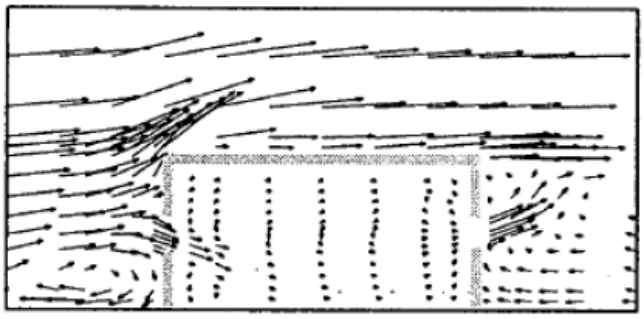

Figure 6: Airflow velocity vectors from wind tunnel experiment [4,5].

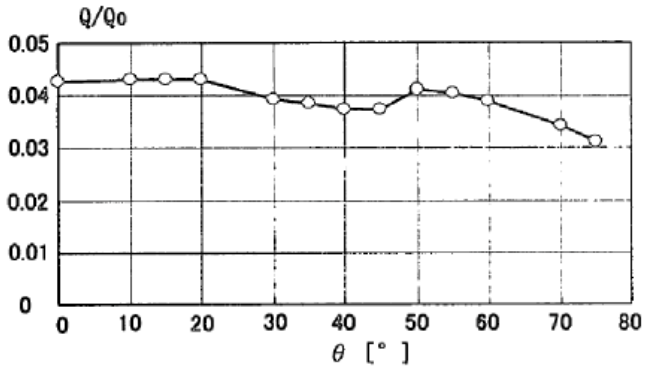

Figure 7: Cross-ventilation rates from wind tunnel experiments [4,5].

Table 1: Summary of Boundary Conditions

Solver	Code-G (Open FOAM)
Analysis area	Three-dimensional space shown in Figure **1**
Inflow conditions	Wind tunnel experiment according to 1/4 power law
Outflow conditions	Free (unrestricted) air flow
Wall treatment	Floor surface: slip, wall function, Z_0 wall function Target building model: Generalized log-law type wall function Other: Slip
Difference scheme	QUICK
Computation Algorithm	SIMPLE

2.2. Verification of Approaching Flows

The profiles of the approaching flows with varying roughness parameter (roughness coefficient) Z_0 are shown in Figure **8**; and under different floor-surface boundary conditions shown in Figure **9**. The building model was omitted and calculations were performed to determine the inflow conditions and the roughness parameter Z_0. The sum of squares of differences in the wind speed profiles in the center of the building is the minimum value. In the airflow-around-building analysis, Z_0 =0.0041 was used for the roughness parameter, while the ventilation airflow analysis used Z_0 = 0.0026.

To compare the results from the airflow-around-building analysis and those from the ventilation airflow analysis individually with their corresponding experimental results, the inflow conditions specific to each of these analyses were used. Figure **9**, shows maximum wind speed differences between the inlet at the floor surface and the airflow in the building for the slip boundary conditions. The difference in wind speeds becomes smaller with the wall function, and is smallest using the Z_0-type wall function.

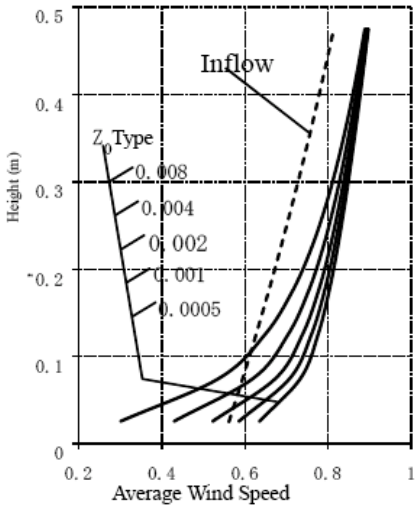

Figure 8: Comparison of approaching flow with varying Z_0 values.

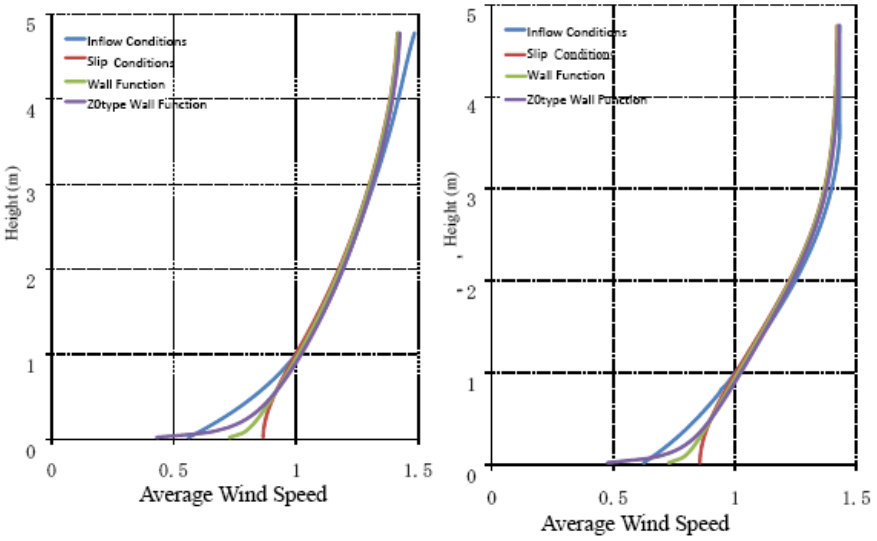

Figure 9: Comparison of approaching flows with the varying wall surface conditions; left: airflow-around-building analysis, right: cross-ventilation airflow analysis.

2.3. Comparison of Results from Calculations with Different Convergent Points

To attain reliable results, data must be obtained from calculations that have reached reasonable convergence. Generally it is possible to determine convergence from residuals in each calculation step. However if a residual plot shows that the residuals are unstable, fluctuating, or do not reach a sufficient residual level, then convergence must be determined on the basis of intermediate results of the calculations. Thus, in this section, results taken at different number of iterations will be compared. The results from the Z_0-type wall function and the SST k–ω model were used. Analyses were performed with the angles of wind direction set to 0° and 45°. The results were extracted from calculations, for which the number of iterations were 500, 1000, 1500, 2000, 2500, and 3000 from the initial conditions.

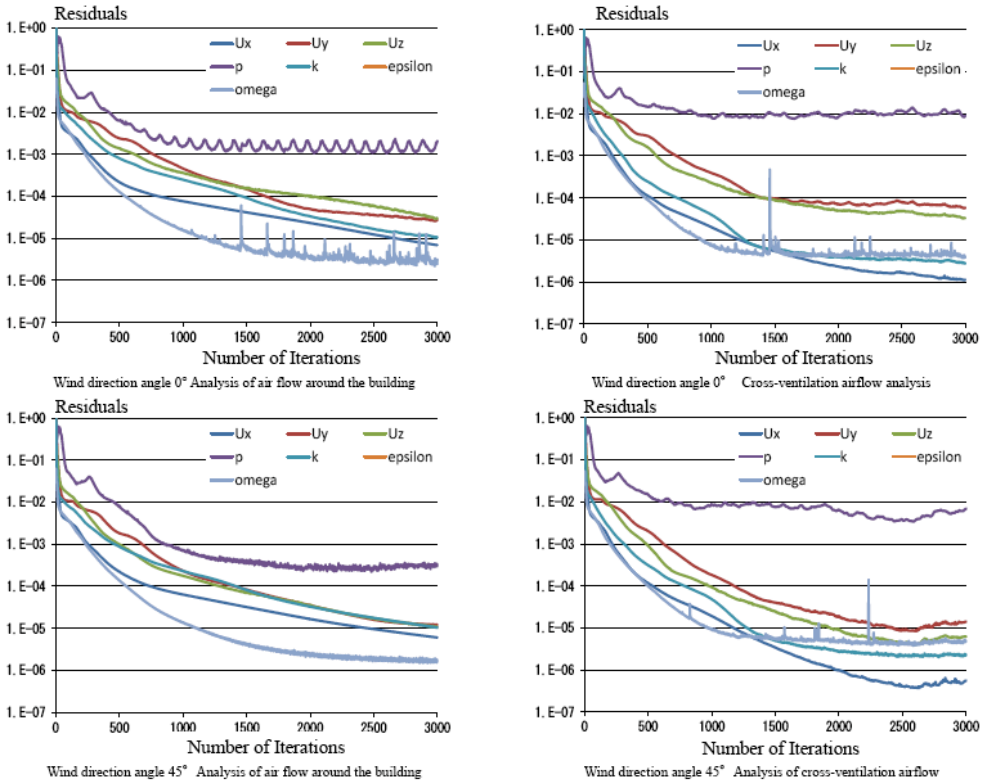

Figure 10: Residuals in airflows around the building (left) and in cross-ventilation flows (right) at wind directions of 0° (upper panels) and at 45° (lower panels).

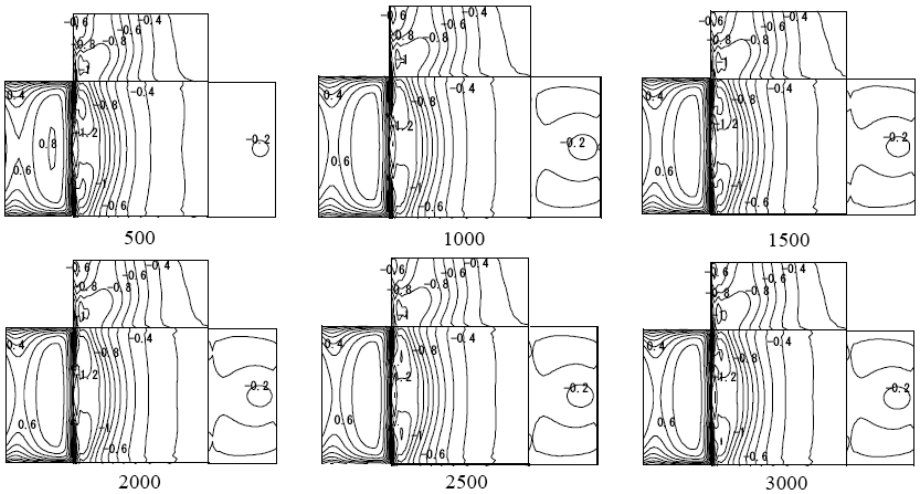

Figure 11: Wind pressure coefficient distribution (angle of wind direction: 0°).

2.3.1. History of Residuals

Figure **10** shows the residual histories from the airflow-around-building and ventilation airflow analyses. The residuals in pressure *p* become almost constant small fluctuations after a given number of iterations.

2.3.2. Comparison of Results by Means of Distributions of Wind Pressure Coefficients

Figures **11** and **12** show how distributions of the wind pressure coefficients vary with the number of iterations. Compared with the experimental data, differences are observed in the upwind area at 500 iterations for the angle of wind direction of 0°; however, at 1000 or more iterations, almost no difference is observed in the upwind area. Slight differences are observed between the distributions on the roof surface at the front edges, but with 2000 or higher iteration factors, the results agree roughly with each other. For the wind direction of 45° differences are observed at 500 iterations, but for 1000 and more iterations, no significant difference is found.

2.3.3. Comparison of Turbulence kinetic Energy Distribution

Figure **13** shows a comparison of the turbulence kinetic energy (*k*) distributions. There were no significant differences between the different iteration cases, and for 1500 or more iterations, almost no differences were found in the results.

Table **2** is a quantified list showing the analyzed results. Although differences are observed in “wind pressure coefficient” and “ventilation airflow” with 500 iterations, almost no differences are found between in the results with 1000 or more iterations. Furthermore, there was little difference in the maximum value of the turbulence kinetic energy or in the reattachment lengths.

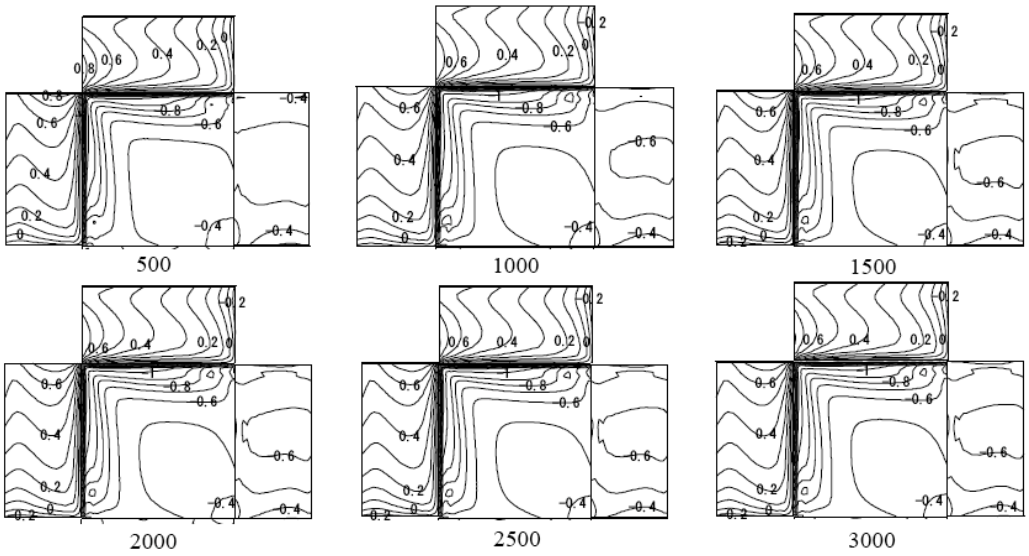

Figure 12: Wind pressure coefficient distribution (angle of wind direction: 45°).

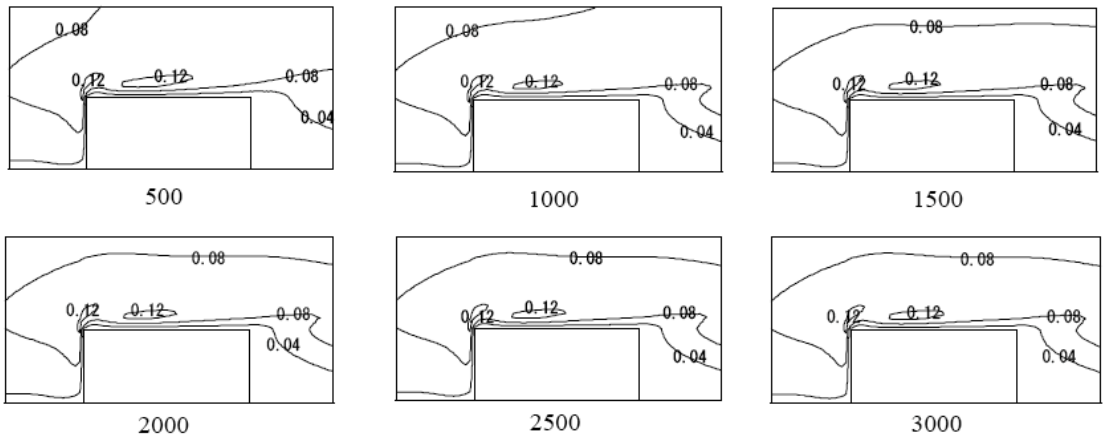

Figure 13: Turbulence kinetic energy (*k*) distributions.

Table 2: Relative Evaluation List as Function of Number of Iterations

		Wind pressure coefficient (0°)			Turbulence kinetic energy (*k*)	Reattachment point		Cross-ventilation air flow	
		maximum	Front Surface Max. Value is distributed around the center area	Roof Surface Min. value is evenly distributed over the front edges	maximum	On the roof	Wake flow	Descent of flow	Cross-ventilation air flow rate
Experiment		0.8 – 0.9	○	○	Approximately 0.1	0.27	1.6	○	0.043
Number of Iterations	500	0.81	×	○	0.13	0.83	2.4	×	0.048
	1000	0.78	○	○	0.13	0.80	2.4	○	0.041
	1500	0.78	○	○	0.13	0.81	2.4	○	0.042
	2000	0.79	○	○	0.13	0.81	2.4	○	0.041
	2500	0.79	○	○	0.13	0.81	2.4	○	0.042
	3000	0.79	○	○	0.13	0.82	2.4	○	0.042

2.3.4. Comparison of Results by Means of Wind Speed Vector Distributions

Figure **14** shows the wind velocity vectors in the XZ (vertical) cross-sections with wind direction of 0° where the airflow runs downward in all the cases with diffused air at the inlet in some cases. Figure **15** shows the diagrams of wind velocity vectors in the XY (horizontal) cross-sections with wind direction of 0°. Figure **16** shows the distributions of wind velocity vectors in the XY (horizontal) cross-sections with wind direction of 45°.

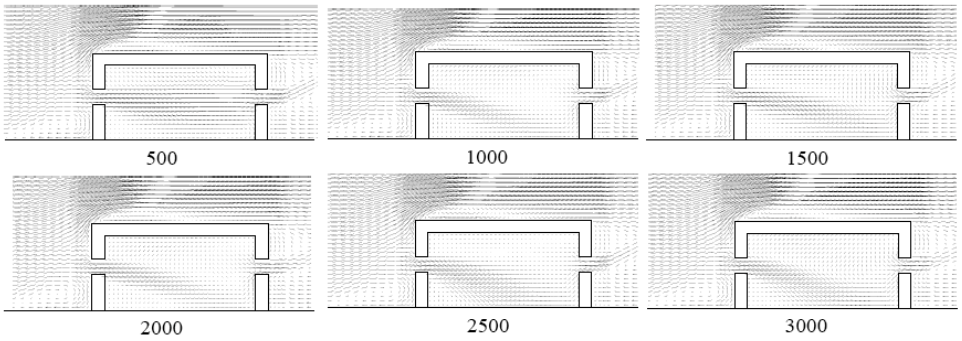

Figure 14: XZ cross-sectional distributions of wind speed vectors (angle of wind direction: 0°).

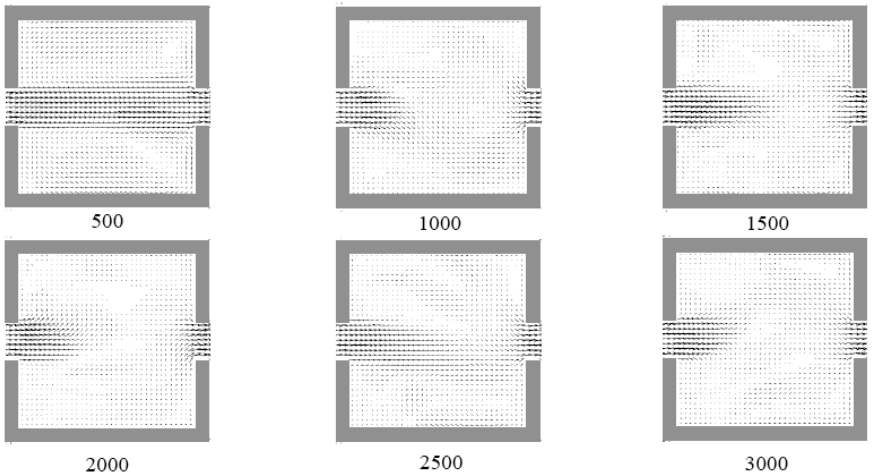

Figure 15: XY cross-sectional distributions of wind speed vectors (angle of wind direction: 0°).

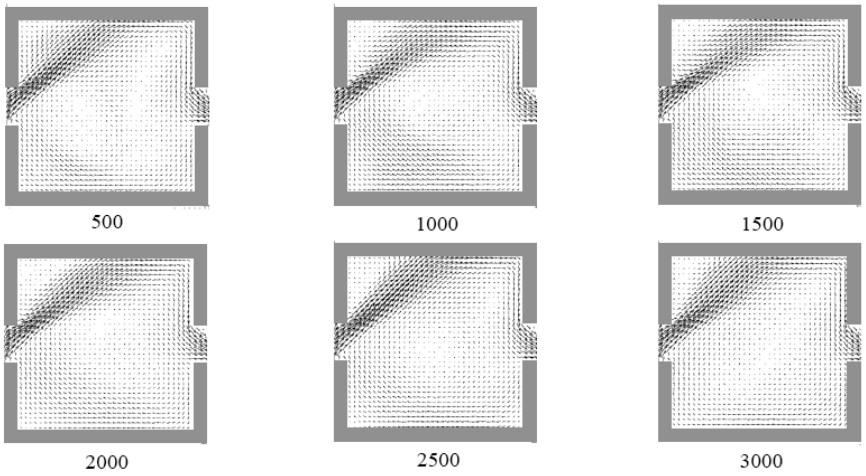

Figure 16: XY cross-sectional distributions of wind speed vector (angle of wind direction 45°).

2.4. Influence of Boundary Conditions for the Floor Surfaces

For an approaching flow, the initial conditions should be based on the inflow surface of the analysis area. The wind velocity profiles at the target building may be different from those of the air inflow initial condition which greatly affects the results [6]. In this section, evaluations are conducted on how the airflow around low-rise buildings and ventilation airflow inside the buildings are affected by different floor-surface boundary conditions.

2.4.1. Analysis Outline

Three types of floor-surface boundary conditions were used: slip, generalized log-law type wall functions, and Z_0-type wall functions. Four turbulence models were also tested: the standard k–ε model, RNG k–ε model, realizable k–ε model, and the SST k–ω model. The analyses were conducted on the airflow-around-the building and inside ventilation airflow at two different wind directions (0° and 45°). Other boundary conditions were the same as those in Table **1**.

2.4.2. Wind Pressure Coefficient Distribution Comparison

Figures **17** and **18** show the wind pressure coefficient distributions for the different setup. Under the slip conditions and wind direction of 0°, a decreasing wind pressure coefficient (compared with the wind tunnel experiment) is not observed in the vicinity of the floor surface on the upstream side of the building. However for the generalized log-law type wall function and Z_0-type wall function, this decrease is found for all turbulence models used. Thus, the circulation, which occurred in the lower part of the building's upstream surface in the wind tunnel experiment, is reproduced with the wall function and Z_0-type wall function. In addition, the maximum value for the pressure coefficient of the building's upstream surface is distributed over the central area, and this result is reproduced using the SST k–ω model with the Z_0-type wall functions.

For a wind direction of 0°, the wind pressure coefficient distribution pattern for the roof surface and building's upstream surface in the SST k–ω model were most approximate to the experimental data. For a wind direction of 45°, the positive pressure on the upstream surface was generally higher for all turbulence models, compared with that obtained from the wind tunnel experiment. However, in the SST k–ω model, the wind pressure was the lowest of all turbulence models, thus matching most closely with the measured data.

2.4.3. Turbulence kinetic Energy Distributions Comparison

Figure **19** shows the turbulence kinetic energy (*k*) distributions where *k* was overestimated using the slip conditions compared against the generalized log-law type wall function and Z_0-type wall function. A decrease in *k* occurred in the vicinity of the floor surface in all turbulence models with the generalized log-law type wall functions or Z_0-type wall functions. The central area around the front edges of the building's roof surface was overestimated for all floor-surface boundary conditions using the standard k–ε and realizable k–ε models. The peak values and the points of peak occurrence in the SST k–ω models were closest to those found in the wind tunnel experiments.

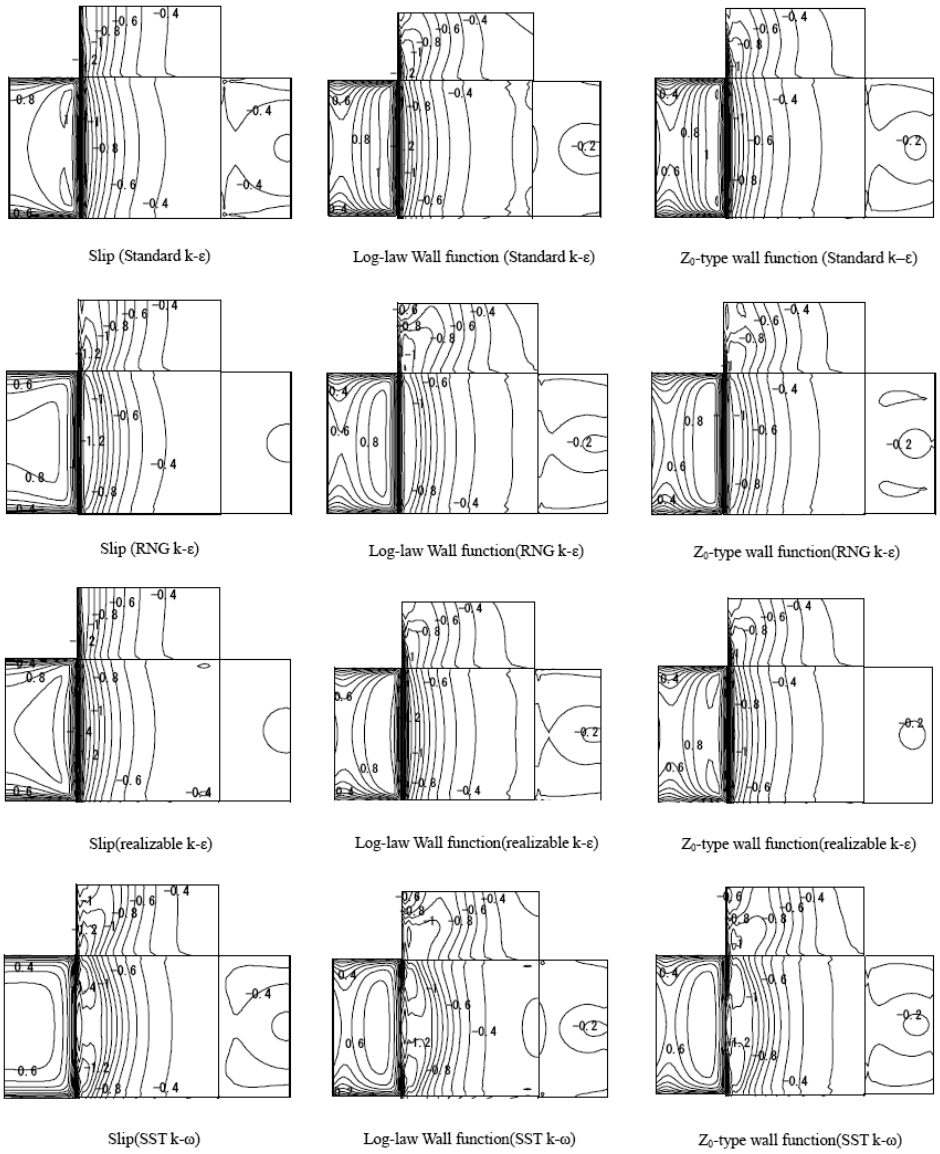

Figure 17: Distributions of wind pressure coefficients (angle of wind direction 0°).

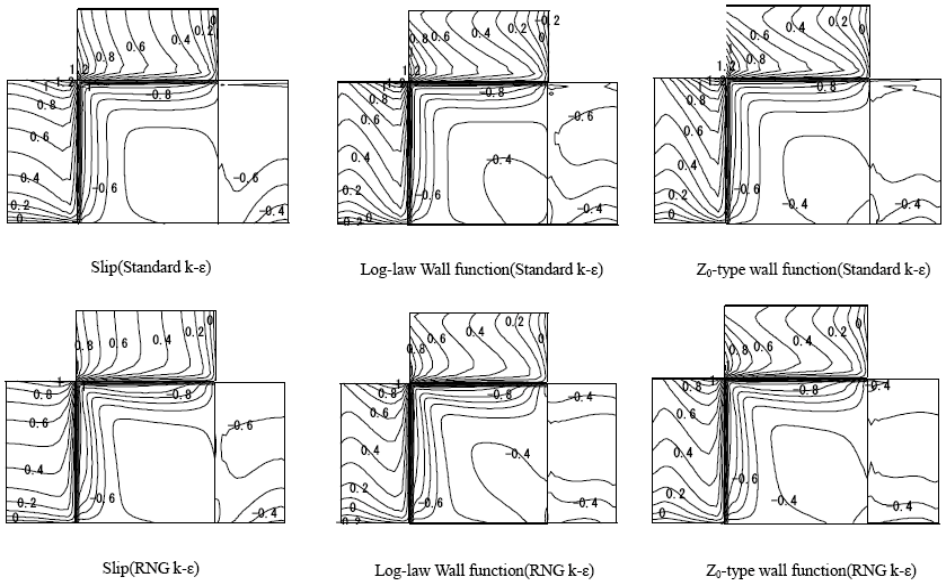

(**Figure 18 Continue**)

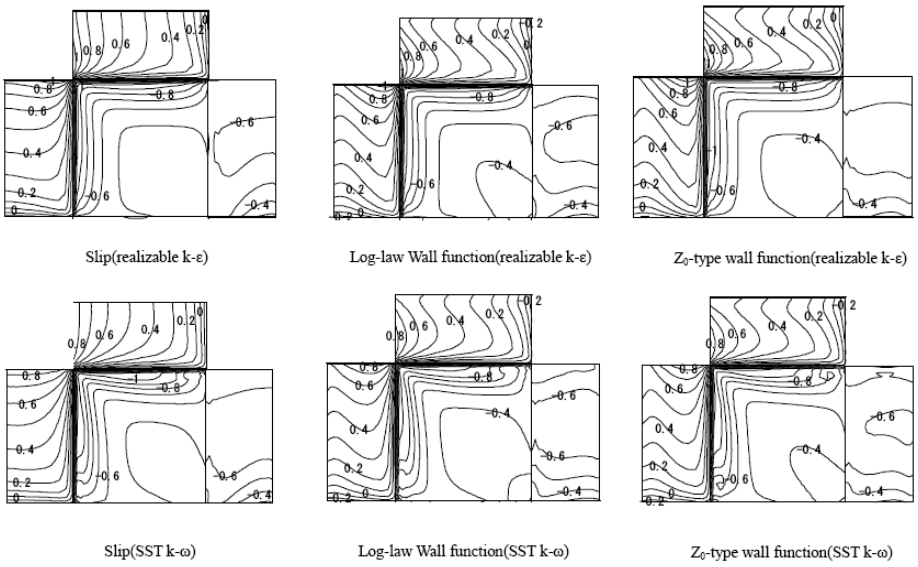

Figure 18: Distributions of wind pressure coefficients (angle of wind direction 45°).

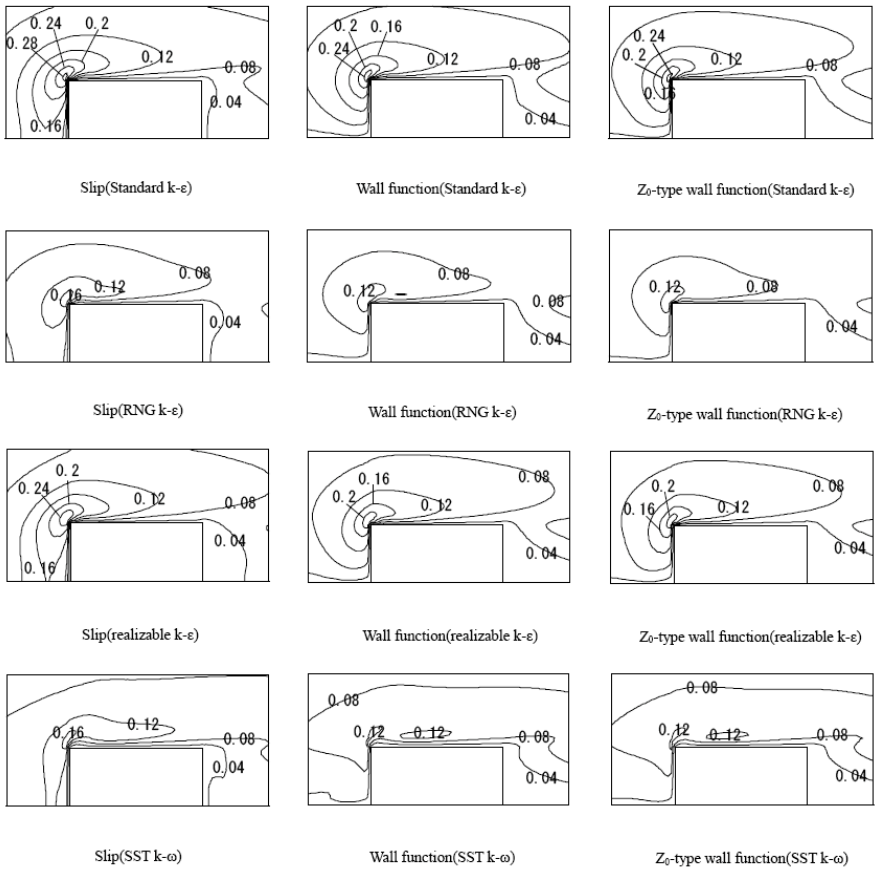

Figure 19: Turbulence kinetic energy (*k*) distribution comparisons.

2.4.4. Comparison of Results by Means of Vortices in Roof Surface Circulation

Figure **20** shows streamlines (flow lines) separated from the roof surface. Although there are slight indications of swirling vortices in the SST k–ω model, no clear manifestations of swirling vortexes occurred in any of these models. Table **3** compares the airflow around the building for wind direction of 0°. The maximum wind pressure coefficient and turbulence kinetic energy in the SST k–ω model closely match

Table 3: Relative Evaluation List as Functions of Turbulence Model

		Wind pressure coefficient (0°)			Turbulence kinetic energy (*k*)	Reattachment point		Cross-ventilation air flow	
		maximum	Front Surface Max. Value is distributed around the center area	Roof Surface Min. value is evenly distributed over the front edges	maximum	On the roof surface	Wake flow	Descent of flow	Cross-ventilation air flow rate
Experiment		0.8 – 0.9	○	○	Approximately 0.1	0.27	1.6	○	0.043
Slip wall	Std k-ε	1.19	○	×	0.30	×	1.8	×	0.041
	RNG k-ε	0.90	×	×	0.18	×	1.8	×	0.045
	Realizable k-ε	1.05	×	×	0.28	×	2.0	×	0.042
	SST k-ω	0.84	×	○	0.18	0.80	2.1	×	0.043
Generalized log-law type wall function	Std k-ε	1.23	×	×	0.26	×	2.2	○	0.040
	RNG k-ε	0.91	○	×	0.16	×	2.2	○	0.041
	Realizable k-ε	1.01	×	×	0.24	×	2.4	×	0.042
	SST k-ω	0.82	○	○	0.13	0.88	2.3	○	0.041
Z_0 type wall function	Std k-ε	1.28	×	×	0.26	×	2.2	○	0.040
	RNG k-ε	0.97	○	×	0.16	×	2.3	○	0.041
	Realizable k-ε	1.07	×	×	0.23	×	2.4	×	0.042
	SST k-ω	0.84	○	○	0.13	0.81	2.4	○	0.041

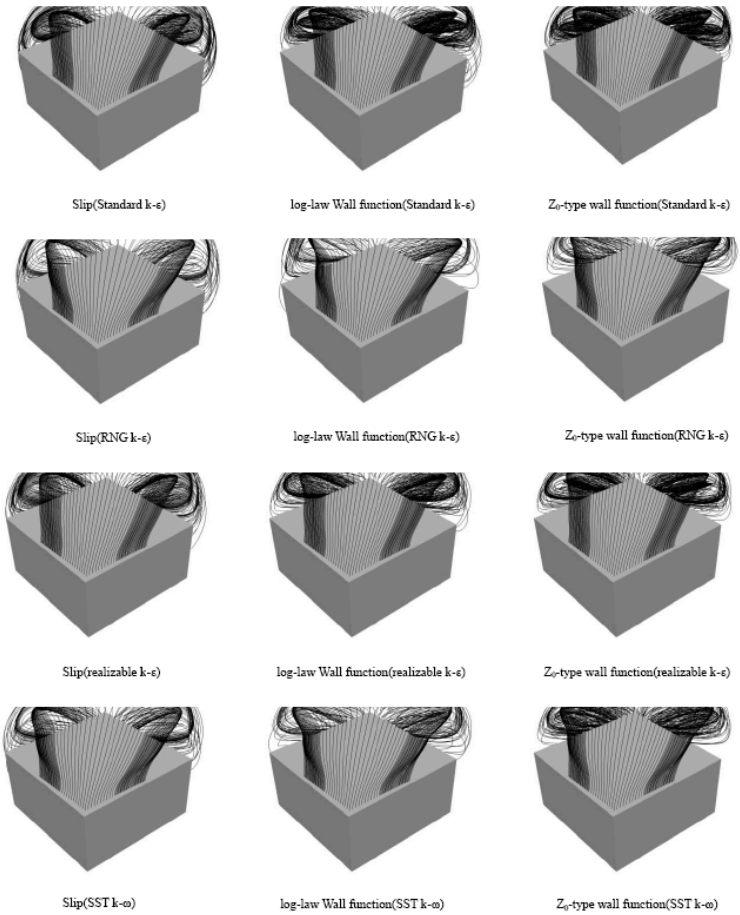

Figure 20: Roof surface circulation vortices.

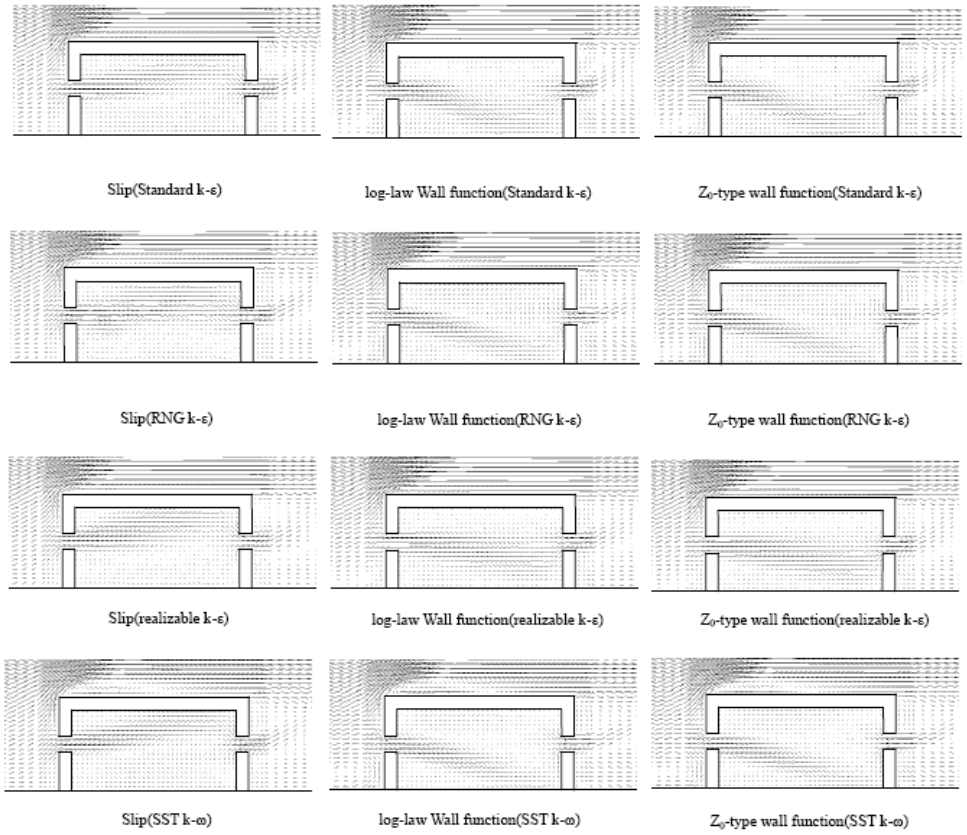

Figure 21: Wind speed vector XZ cross-sectional diagram (angle of wind direction 0°).

Table 4: Relation Between Cross-Ventilation Volume and the Angle of Wind Direction

Cross-ventilation rate		Wind direction angle [°]					
		10°	22.5°	30°	45°	60°	70°
Slip wall	Std k-ε	0.029	0.030	0.030	0.031	0.028	0.023
	RNG k-ε	0.030	0.031	0.030	0.030	0.028	0.023
	Realizable k-ε	0.029	0.030	0.030	0.031	0.029	0.023
	SST k-ω	0.030	0.031	0.031	0.030	0.030	0.024
Generalized log-law type wall function	Std k-ε	0.028	0.030	0.030	0.027	0.029	0.024
	RNG k-ε	0.031	0.030	0.030	0.029	0.028	0.023
	Realizable k-ε	0.030	0.031	0.030	0.029	0.029	0.023
	SST k-ω	0.031	0.032	0.031	0.030	0.030	0.024
Z_0 type wall function	Std k-ε	0.028	0.032	0.029	0.029	0.028	0.023
	RNG k-ε	0.030	0.029	0.030	0.029	0.028	0.023
	Realizable k-ε	0.030	0.030	0.030	0.029	0.028	0.023
	SST k-ω	0.032	0.031	0.031	0.029	0.029	0.024

those found in the wind tunnel experiments. In all cases, the wake flow was overestimated in terms of the reattachment lengths for the separated airflow. Although the reattachment points for the roof surface only reappeared in the SST k–ω model, it was still overestimated in the same manner as the wake flow. There were no significant differences or variations in cross-ventilation volume (ventilation air flow rate) found between the analyzed cases, and the cross-ventilation volume was generally the same as that found in the wind tunnel experiments.

2.4.5. Comparison of Results by Means of wind speed vectors

Figure **21** shows wind velocity vector distributions (XZ cross section) from the inside ventilation analysis. Under slip conditions, the flow moves upwards and through the building from but for log-law type wall

functions and Z_0-type wall functions the flow dips down and emerges from the base of the building for all turbulence models. Aside from the realizable k–ε models, the airflow moved significantly downward (which was found in the measurements).

2.4.6. Comparison of Cross-ventilation Volumes with Different Wind Direction Angles

Table **4** shows the cross-ventilation volumes for different approaching wind directions, and Figure **22** shows the average cross-ventilation volumes for each wind direction. No large variations are observed in the turbulence models under the floor-surface boundary conditions. However, cross-ventilation volumes were underestimated compared with those from the wind tunnel experiments. There were no differences in results between simulations and experimental for wind direction of 0^o. This suggests that issues may arise in the computational mesh used in the analyses when the wind direction varied. Figure **22** shows a smaller cross-ventilation volume compared with the experiment. As the angle of wind direction increased, the cross-ventilation volume decreased which was observed in the experiment.

2.5. Influence of Mesh Design

The computational mesh used in this analysis was created like a turntable around the building in the same way as in the wind tunnel experiments. To take the wind direction into consideration, we rotated the outer mesh and then connected it with the circumference of the turntable mesh. To determine whether the results were affected by the discontinuous mesh on the turntable boundary, results from two experiments; one using a turntable with 2 as radius (normal) and the other using a turntable with 5 as radius (representative length scale in this analysis is building height (=1)). Figure **23** shows the grid design around building model and turntable.

2.5.1. Outline of Analysis

The following four turbulence models were tested: standard k–ε, RNG k–ε, realizable k–ε, and SST k–ω models. Computations were performed at wind direction of 0° and 45°. All three boundary conditions, slip, wall function, and Z_0-type wall function, were used for floor-surface conditions in the SST k–ω model. The other three turbulence models were tested using just the Z_0-type wall function.

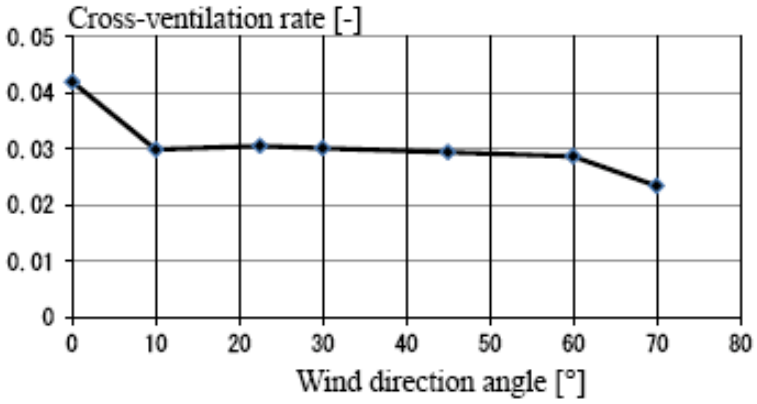

Figure 22: Cross-ventilation volume at different angels of wind directions.

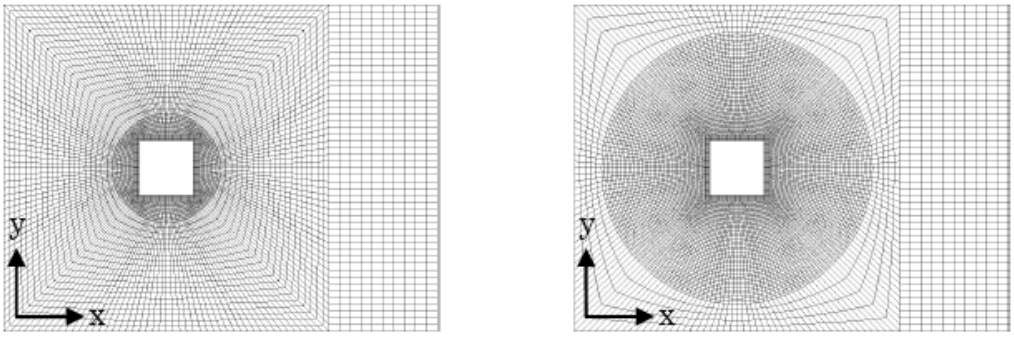

(**a**) (**b**)

Figure 23: Mesh design for the turntable analysis regions (**a**) radius = 2, (**b**) radius = 5.

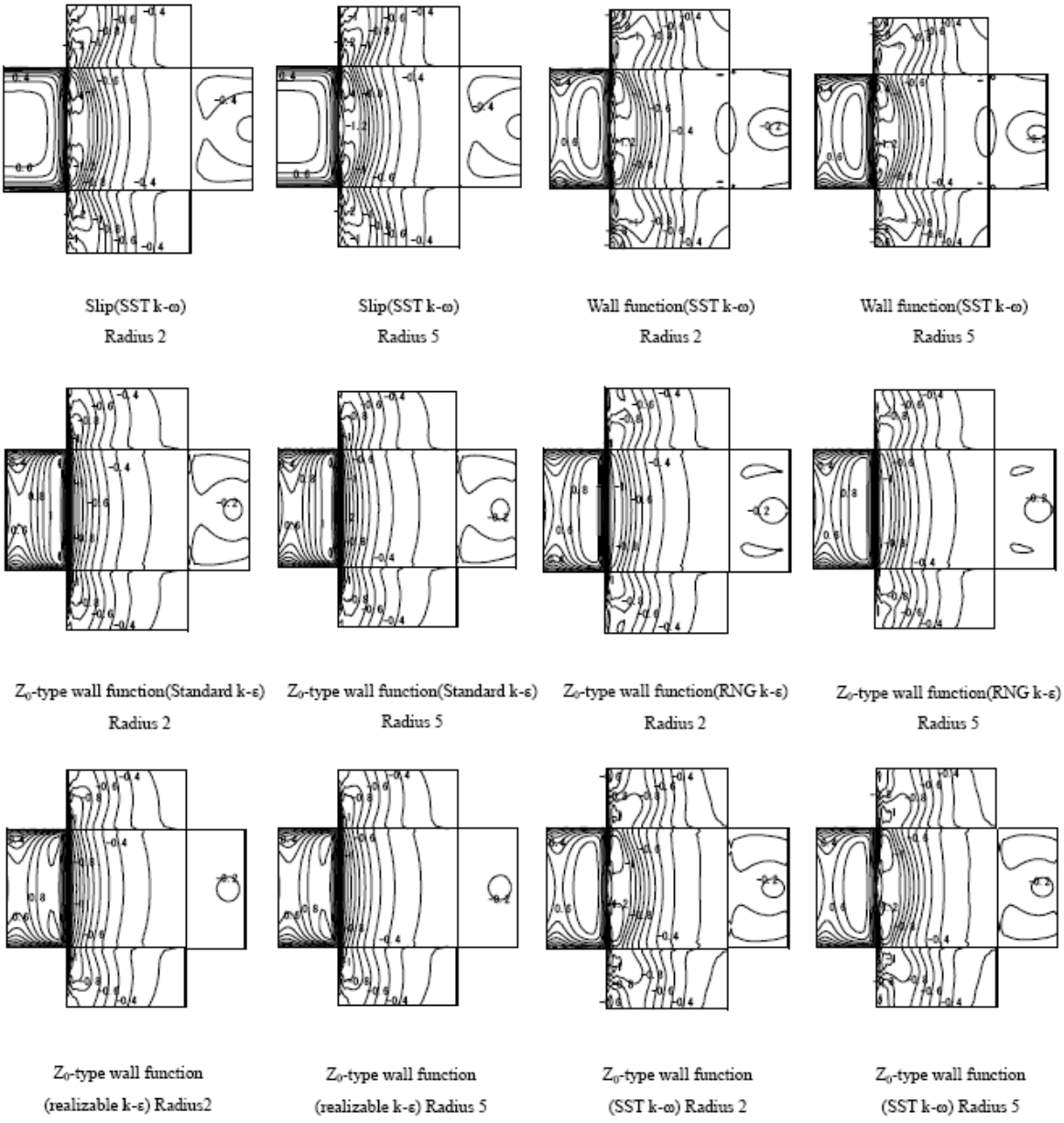

Figure 24: Distributions of wind pressure coefficients for a wind direction of 0°.

2.5.2. Comparison of Simulation Results

Figures **24** and **25** compare distributions for wind pressure coefficients at directions of 0° and 45°, respectively. Slight variations are observed in the results using (1) wind direction of 45°, (2) the wall function, and (3) the SST k–ω model. However, no significant differences are observed in any of the other cases.

Figure **26** shows turbulence kinetic energy (*k*) distributions derived from the analysis results. None of the analyzed cases show any large differences between the results. Table **5** shows the maximum values for the turbulence kinetic energy and wind pressure coefficient, and the distance to reattachment points for the separation airflow. The maximum values for turbulence kinetic energy and wind pressure coefficient were almost the same in all the cases, and there were no significant differences in the distance to a reattachment point in either the wake flow or roof surface.

Figures **27-29** show the wind velocity vectors where the XZ cross-sectional results show slight diffusion of the air inflow depending on the mesh radius (2 or 5). Although the XY cross-sectional results also show slight differences depending on the angle of wind direction (0° or 45°), the results were similar.

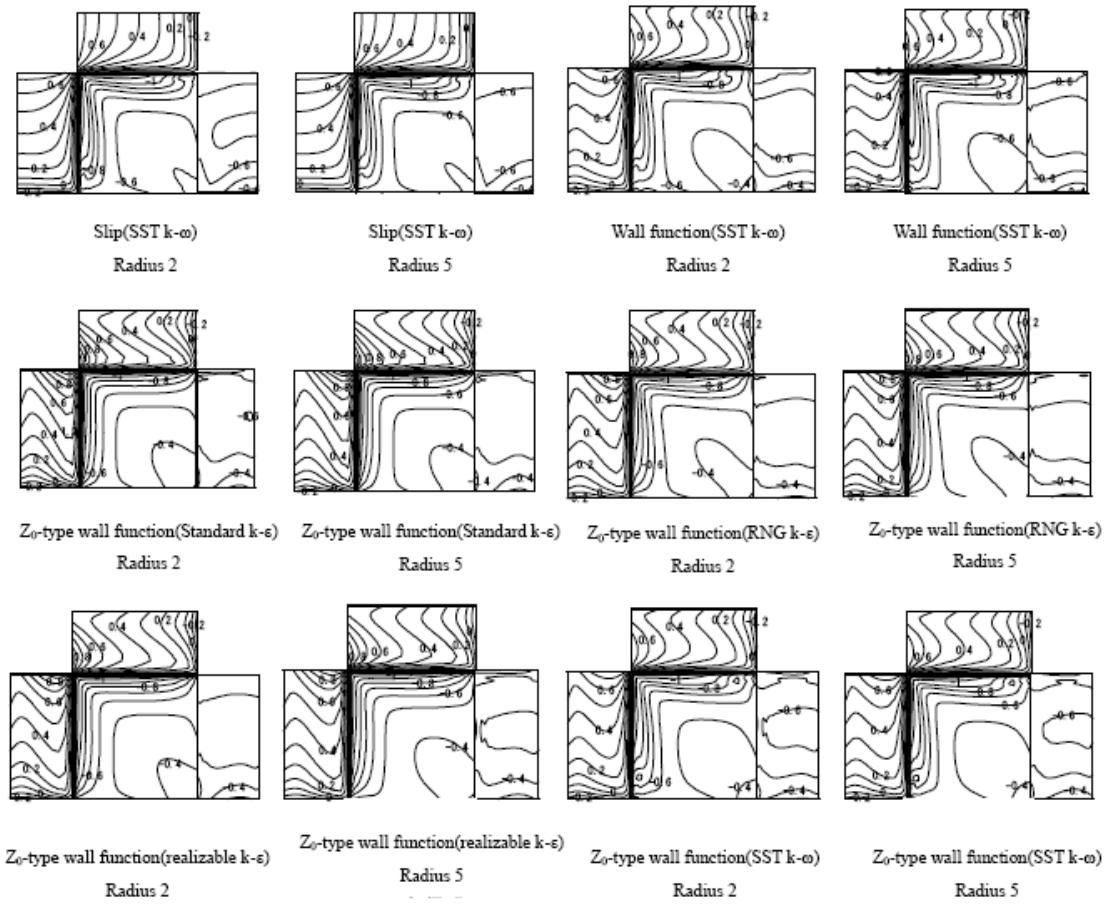

Figure 25: Distributions of wind pressure coefficients for the angle of wind direction of 45°.

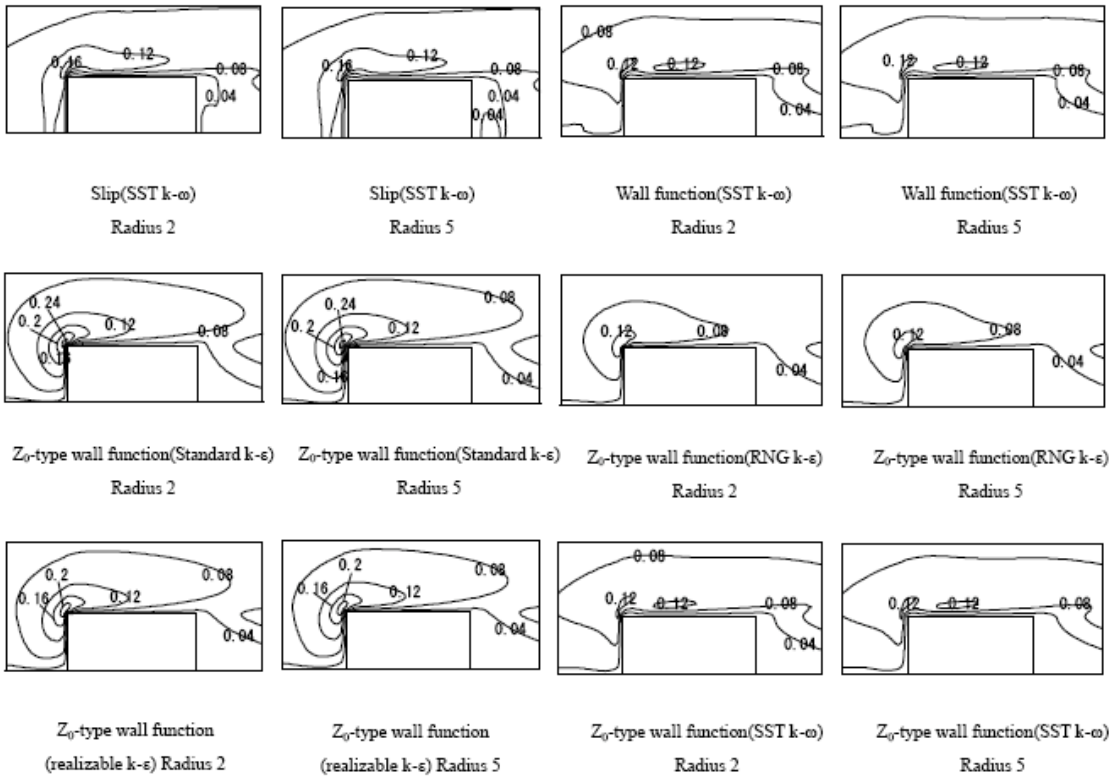

Figure 26: Turbulence kinetic energy (*k*) distributions.

Table 5: Comparison Table

		Pressure coefficient Max. value		Turbulence kinetic energy Max. value		Re-attachment – Roof surface		Re-attachment – Wake flow	
Floor surface	**Turbulent model**	**Radius 2**	**Radius 5**	**Radius 2**	**Radius 5**	**Radius 2**	**Radius 5**	**Radius 2**	**Radius 5**
Slip	SST k-ω	0.79	0.79	0.18	0.18	0.80	0.79	2.05	2.03
Wall function	SST k-ω	0.76	0.76	0.13	0.13	0.88	0.90	2.29	2.38
Z0 type	Stand k-ε	1.11	1.12	0.26	0.26	-	-	2.23	2.26
	RNG k-ε	0.89	0.89	0.16	0.16	-	-	2.34	2.39
	Realizable k-ε	0.93	0.93	0.23	0.23	-	-	2.45	2.49
	SST k-ω	0.79	0.78	0.13	0.13	0.81	0.82	2.44	2.52

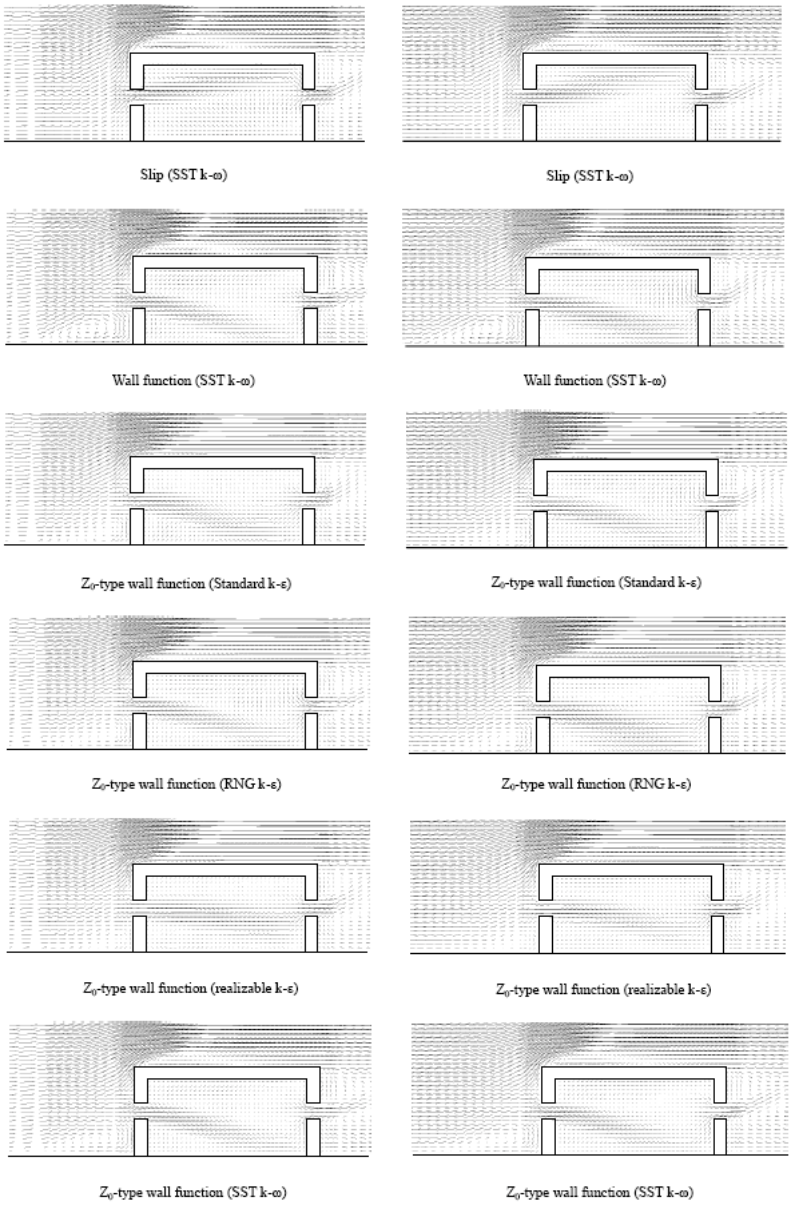

Figure 27: Wind speed vector XZ cross-sectional diagram (wind direction of 0°); left: radius = 2, right: radius = 5.

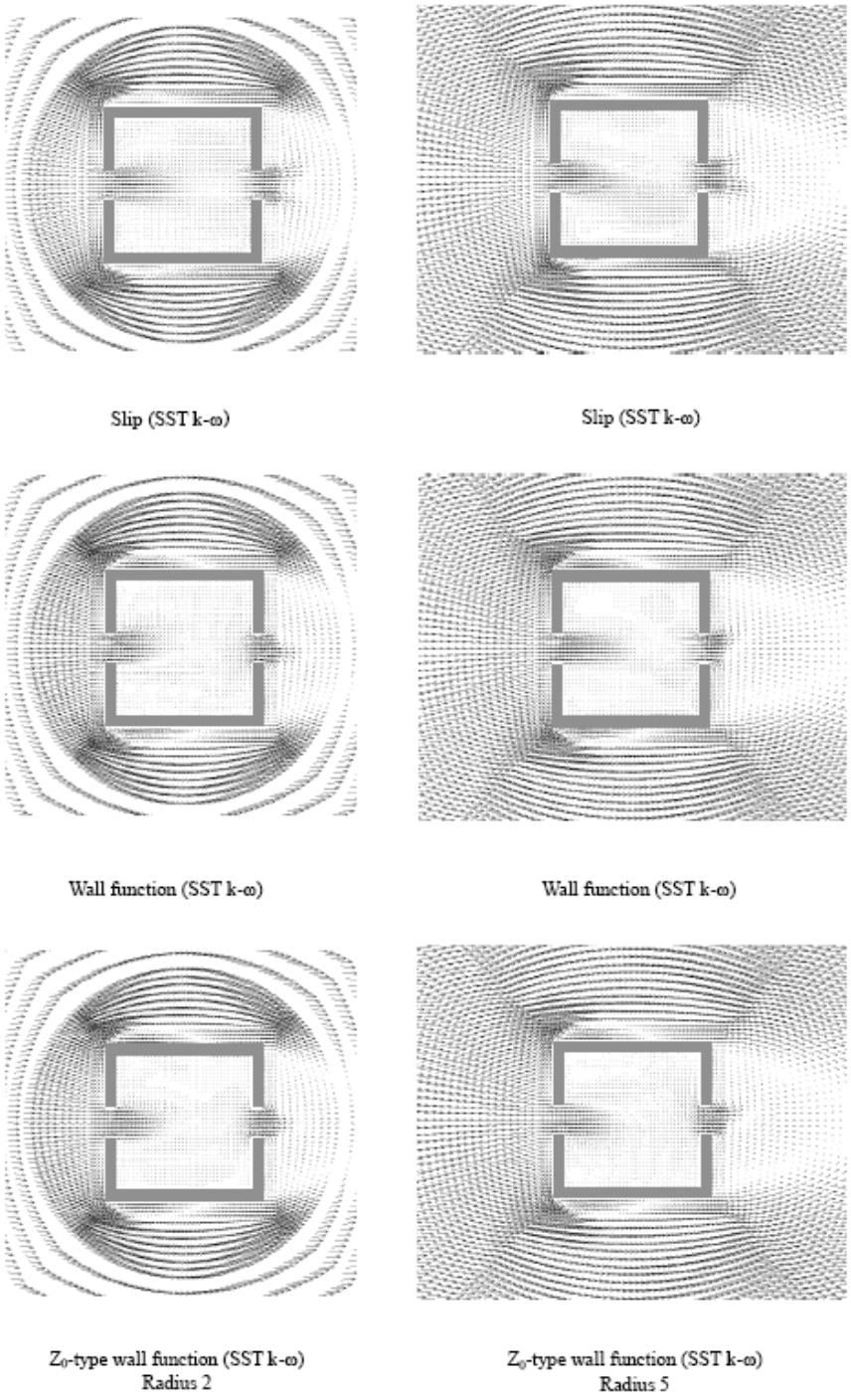

Figure 28: Wind speed vector XY cross-sectional diagram for a wind direction of 0°; left: radius= 2, right: radius= 5.

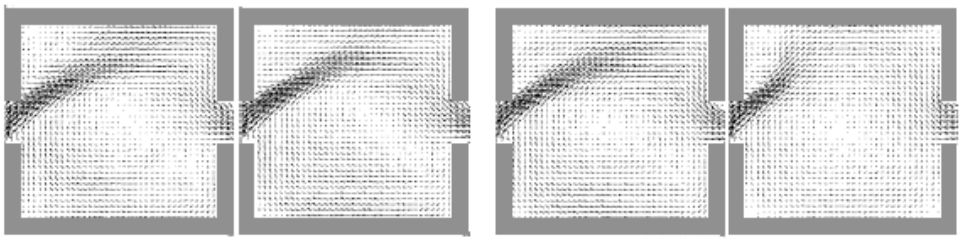

(Figure 29 Continue)

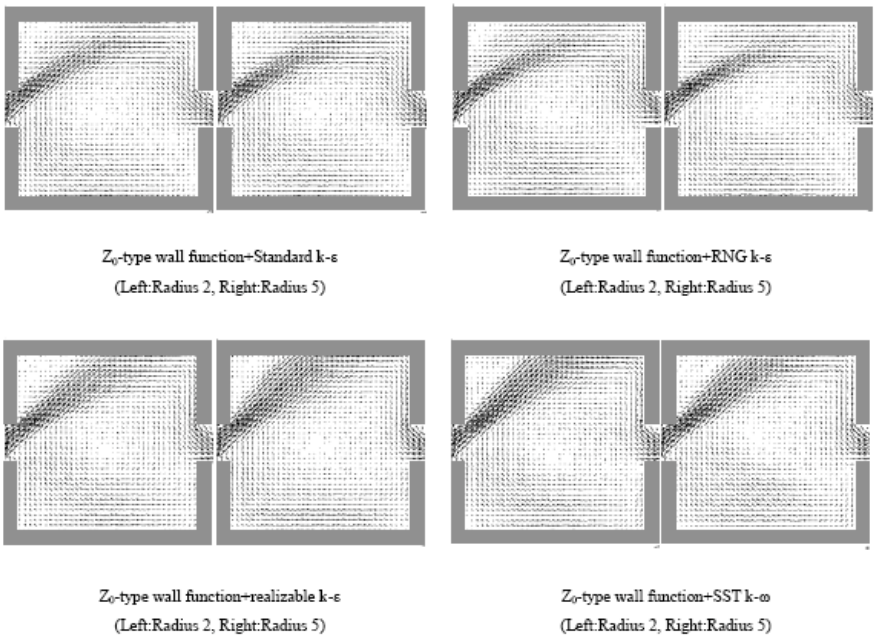

Figure 29: Wind vector XY cross-sectional distributions for the angle of wind direction of 45°.

Table 6: Cross-Ventilation Volumes for the Angle of Wind Direction of 0°.

	Slip	Wall function	Z0- type wall function			
	SST k-ω	SST k-ω	Stand k-ε	RNG k-ε	Realizable k-ε	SST k-ω
Radius 2	0.043	0.041	0.040	0.041	0.042	0.041
Radius 5	0.043	0.042	0.039	0.041	0.041	0.041

Table **6** shows the cross-ventilation volumes obtained from the analysis results. No critical differences are observed in the analyzed cases.

Although slight differences were observed in wind vector diagrams, all other results showed no large differences. These computational results did not appear to be affected by the size of the turntable being more than twice the radius of the building.

2.6. Influence of Relaxation Factor

In general, convergence is related to the setting of relaxation coefficient (relaxation factor), and we can expect better convergence and faster computation speeds when the relaxation factor is set appropriately. We have studied how the history of residuals and computation results respond when the relaxation factor is changed.

2.6.1. Analysis Outline

Analyses were conducted using the Z_0-type wall function and the SST k–ω for the turbulence model, with wind direction of 45°. The relaxation coefficients tested were 0.1, 0.3, and .05, for pressure *p* and for all other scalars (*U*, *k,* ω) were 0.3, 0.5, and 0.7.

2.6.2. Comparison of Simulation results

Figure **30** shows the residual history for different relaxation coefficients. The residuals decrease when the relaxation factors increase. When the relaxation factors (with the exception of pressure) are set to 0.3 and 0.5, slight decreases in the residuals continue to occur after 2000 iterations.

Figure **31** shows wind pressure coefficient distributions based on different relaxation factors. Aside from the pressure *p*, there were some slightly asymmetric areas on the building's leeward surface. However, other wall surfaces and roof surfaces in all of the analyzed cases generally showed the same results.

Figure **32** shows XY cross-sectional diagrams for wind velocity vectors which show changes in the relaxation factor caused differences in airflow diffusivity after the airflow inlet. No further effects were found in the large flow field.

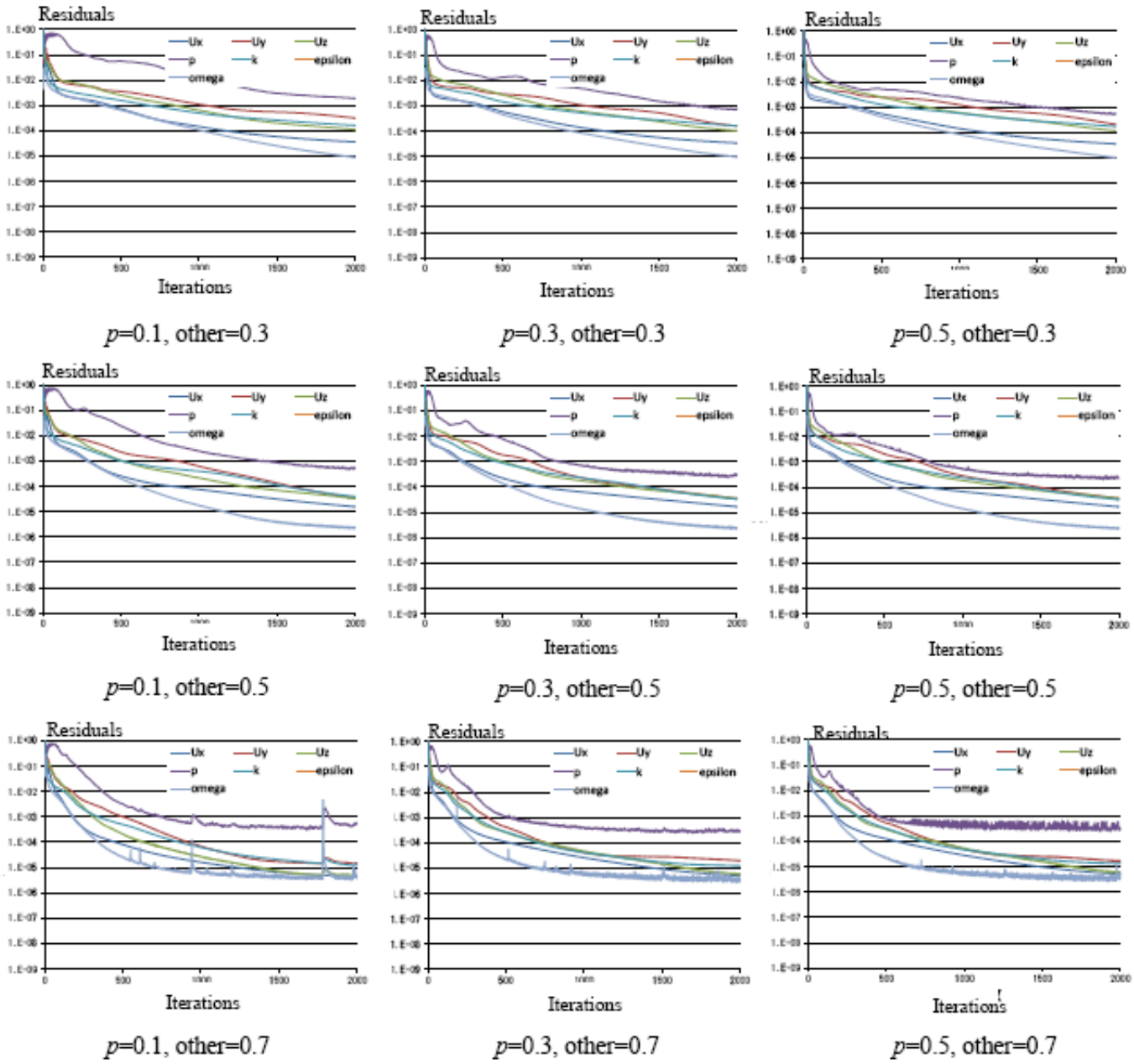

Figure 30: Results of Histories of Residuals.

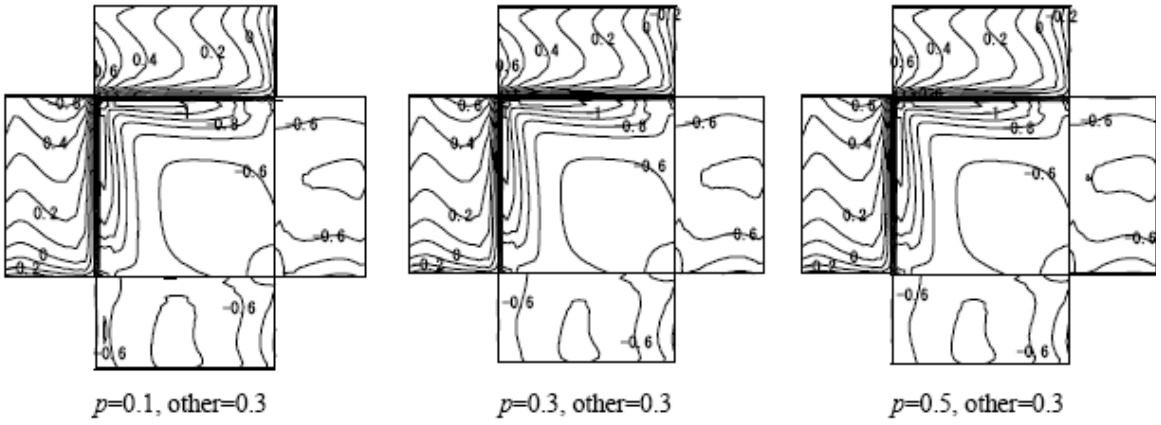

(**Figure 31 continue**)

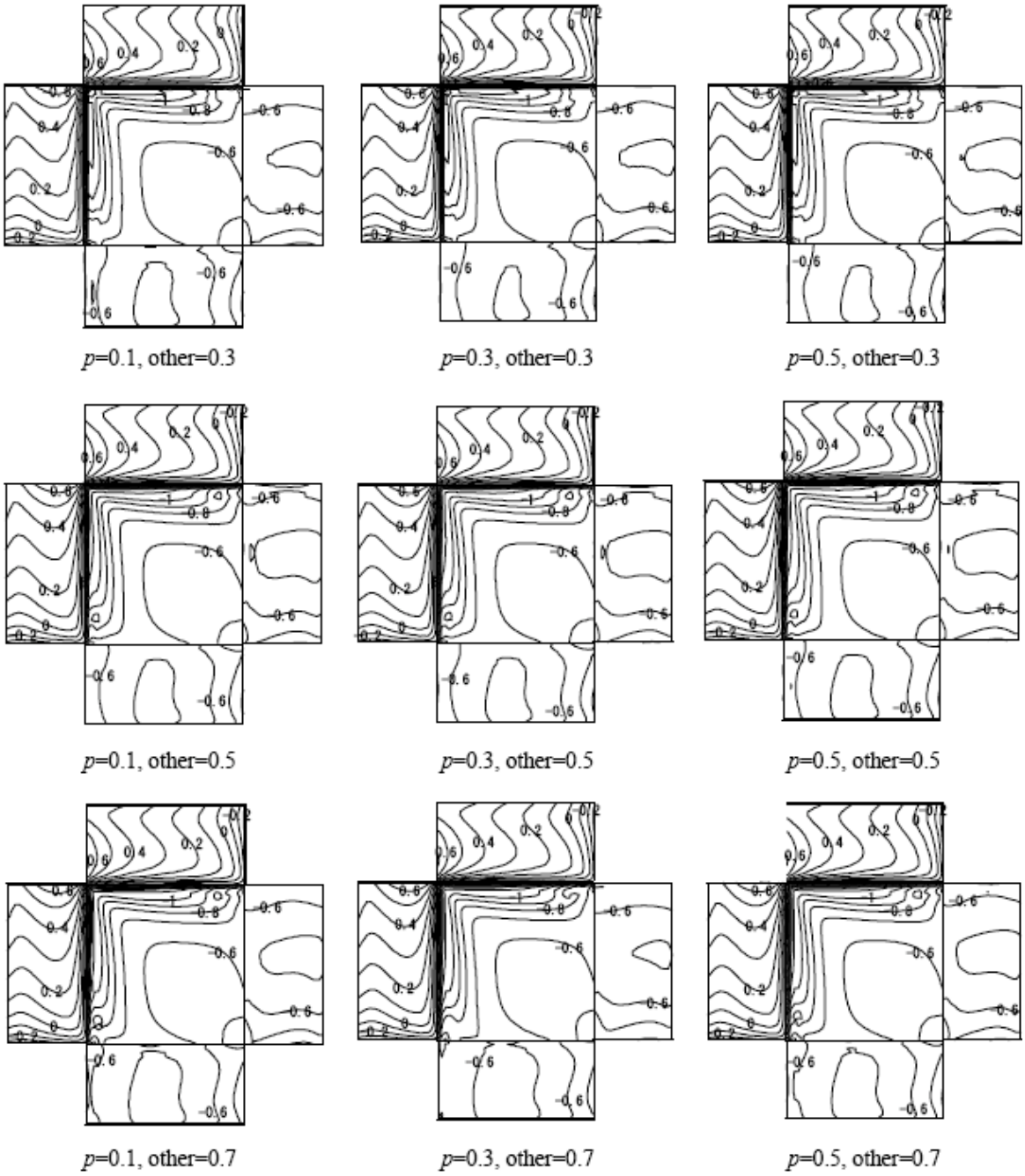

Figure 31: Distributions of wind pressure coefficients.

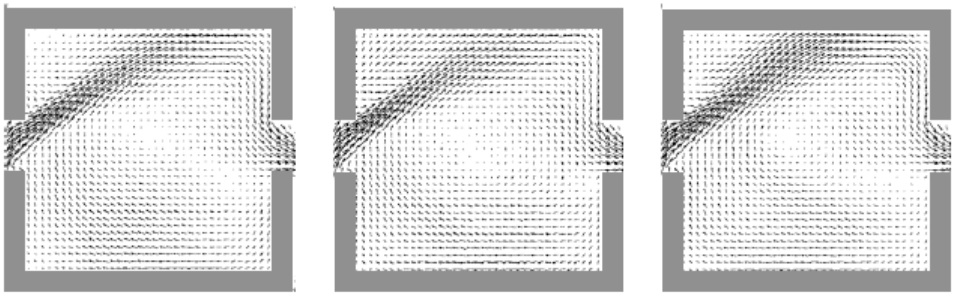

(Figure 32 continue)

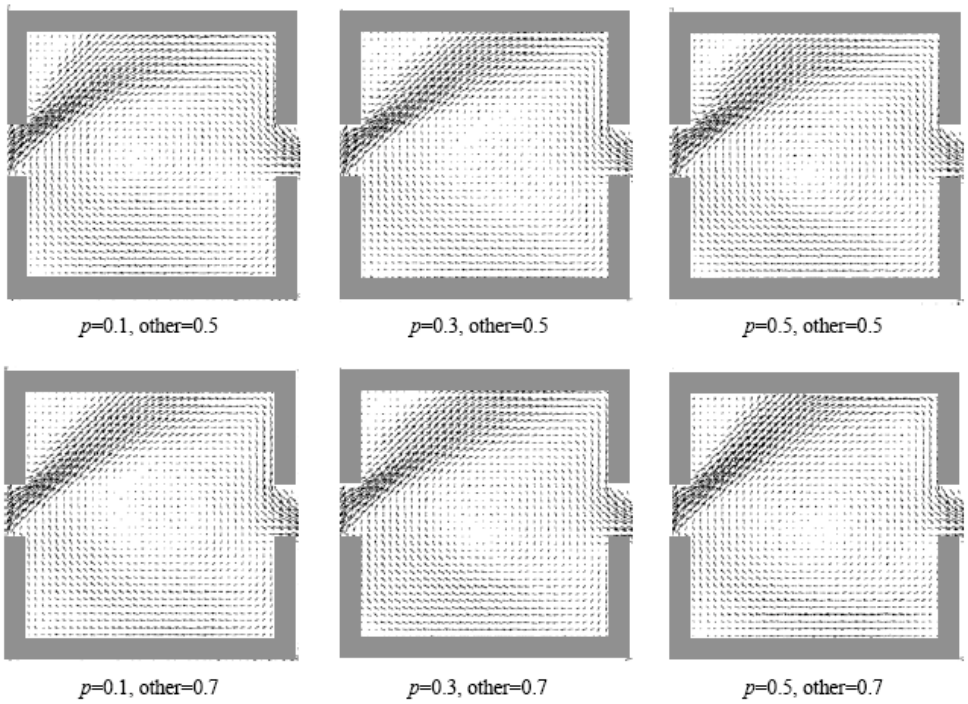

Figure 32: Cross-sectional diagrams for wind speed vectors XY.

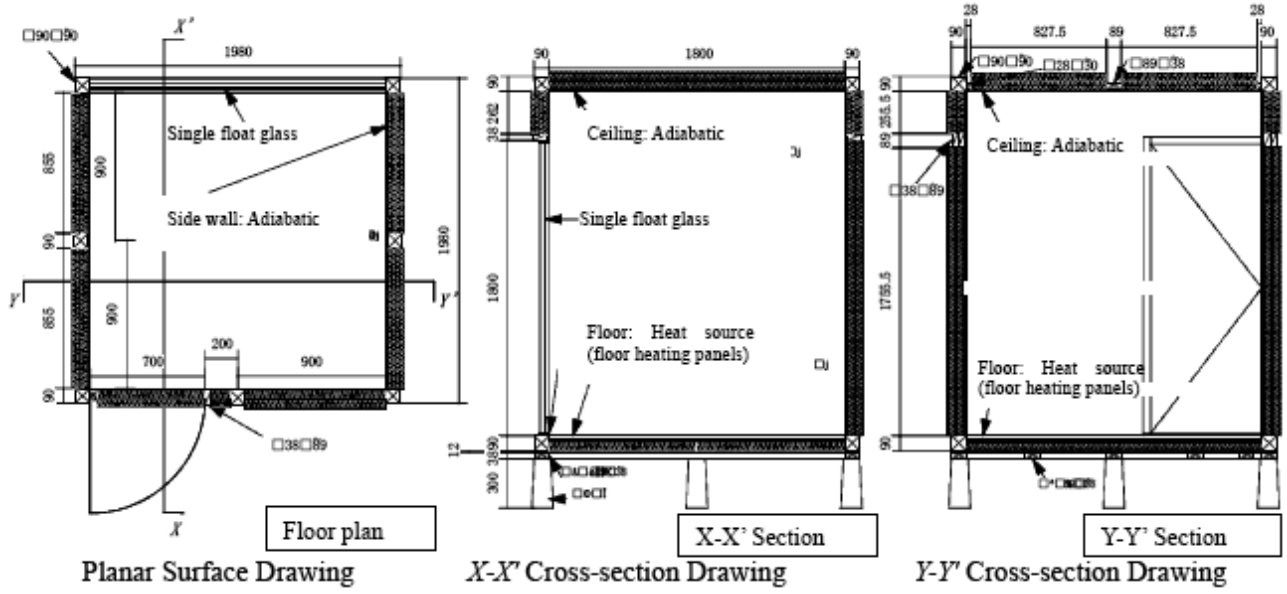

Figure 33: Schematic of the model for a room having floor heating [7].

2.7. Summary of Benchmark tests for Cross-Ventilation

A comprehensive CFD analysis for cross-ventilation flow was performed with OpenFOAM. The highest reproducibility of the predicted results compared with the wind tunnel results occurred when the Z_0-type wall function was used as the floor-surface boundary condition and the SST k–ω for the turbulence model.

Although some differences are observed between the results from calculations with 500 iterations, no significant differences are found when 1000 or more iterations were performed. To determine whether the calculation has reached convergence, it is necessary not only to check the residual history but also to extract intermediate results to verify that no differences are observed even with high iteration number of calculations.

In terms of the relaxation factor, all cases in this study generally produced the same results, although some distributions of air pressure coefficients and wind velocity vectors displayed marginal differences because of changes in relaxation factors. Differences could also be seen in the history of residuals, so we conclude that convergence varies with changes in relaxation factors. Since the overall goal is convergence (even for stages in which a residual declines at a very slow rate), it is important to perform convergence tests while extracting and confirming computational results during intermediate stages.

3. BENCHMARK TEST FOR NATURAL CONVECTION IN A ROOM WITH FLOOR HEATING

3.1. Outline

A database, which contains temperature distribution measured on the full-scale model of a room having floor heating, was used to verify the computational prediction accuracy of a commercial CFD program for an indoor airflow field. Floor heating typically produces unstable stratification in an indoor flow field [7].

3.2. Outline of the Temperature Distribution Database

The temperature distribution database built by Ono *et al*. [7] was used for benchmark test. The model room (Figure **33**) had a floor area of 3.24 m^2 and a ceiling height of 2.1 m and a simplified constant temperature room and electrical heating panels were laid on the floor surface. Single float glass plates, each of which has almost the same area as the floor surface, were used for the window panes. This type of window pane produces a cold draft.

Thermocouples (T-CC) were used to measure wall surface temperatures at 314 points in total and air temperatures at 592 points in total (Figure **34**). In addition, the quantity of heat into the room was calculated on the basis of the power consumed by the heating panels and the rate of heat transfer into or out of the room and the values for radiation and convection components were reported.

3.3. CFD Computational Models

3.3.1. Computational Mesh

Figure **35** shows an overview of the computational mesh which is made of structured hexahedral elements in the center of the room and thinning at the wall surface. The following definitions are applied:

I. the cell width of the mesh in the center area of the room is l_{max};

II. the cell width of the area adjacent to the wall surface is l_{min}, and

III. the maximum enlargement factor for adjacent mesh part is R_{ex}.

Values for these three mesh parameters are given in Table **7**. Taking advantage of the experimental model symmetry, calculations were performed only for half of the right-hand-side of Figure **33**, and the cross section in the middle of the room was chosen as the symmetry boundary.

Table 7: Values used for Computational Mesh Parameters

Name	l_{min} [mm]	l_{max} [mm]	R_{ex}	Total Cell Count
1-25-1.1	1.0	25	1.1	1,045,568
1-50-1 1	1.0	50	1.1	594,880
1-50-1.3			1.3	143,360
1-50-1.5			1.5	97,216
1-50-2.0			2.0	70,000
1-100-1.3	1.0	100	1.3	74,256

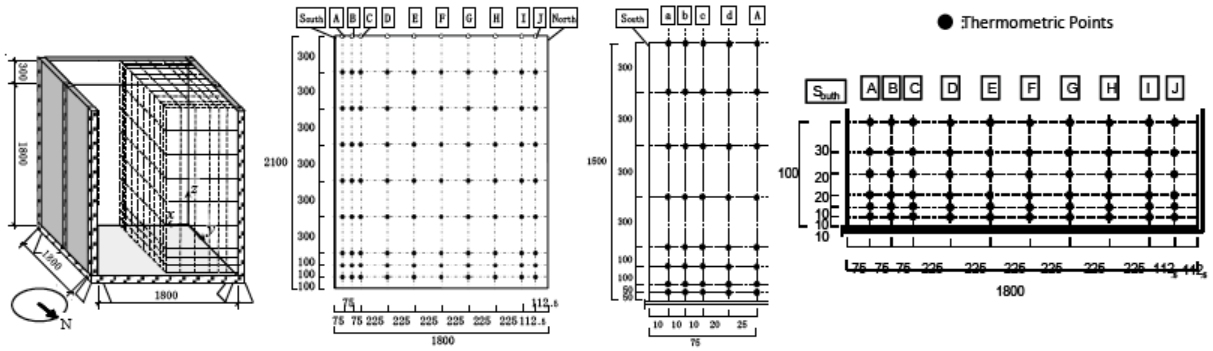

Figure 34: Points at which temperatures were measured (distances in mm) [7].

Table 8: Positions of Monitoring Points

	y [m]	*z* [m]
c-1	0.1	0.1
c-2	0.3	0.1
c-3	0.5	0.1
c-4	0.7	0.1
c-5	0.9	0.1
h-1	1.7	0.1
h-2	1.7	0.5
h-3	1.7	0.9
h-4	1.7	1.3
h-5	1.7	1.7
center	0.9	1.05

3.3.2. Boundary Conditions and Discretization Procedures

Boundary conditions for air velocity and turbulence kinetic energy on wall surfaces were set to no-slip, and the measured temperatures were used (Figure **35**). To discretize advection terms, the second-order accurate TVD scheme was used for velocity and temperature and the first-order upwind difference scheme for turbulence quantities to ensure computational stability. The SIMPLE algorithm was used for steady calculations, and the PISO algorithm (Δt = 0.01 s) for unsteady calculations. Calculations were performed until fluctuations in the time-averaged air temperatures at the monitoring points became sufficiently small. The surface temperature distributions of each wall surface in accordance with the results of room model experiment were precisely applied as Dirichlet type boundary condition.

The air was assumed incompressible, and the Boussinesq approximation was used for the buoyancy term. Code- G (Open FOAM) was used to create the mesh and conduct the CFD simulation. However, an improvement was made such that the buoyancy production term was added to the program.

3.3.3. Turbulence models

The model created by Lien *et al*. [8], hereafter, referred to as LL model, has been incorporated in many commercial software as a low Reynolds number k–ε model, and the k–ω SST model (hereafter, referred to as SST), of which previous version, the k–ω model, was developed by Wilcox [9] and improved by Menter [10], were used for the turbulence model.

3.4. Considerations for Handling Unsteady Flow

In this study, there were cases in which vortices periodically appeared, and steady-state flows did not develop in the flow fields. These unsteady flows generated from unstable thermal stratifications are characteristic of heating produced by floor panels. The measured data showed that the computations did not reach convergence to a single steady solution in the room with the floor heating panels. To address this problem, the optimal procedure for accommodating the simulation time was discussed. This led to identification of three scenarios for addressing the above problem:

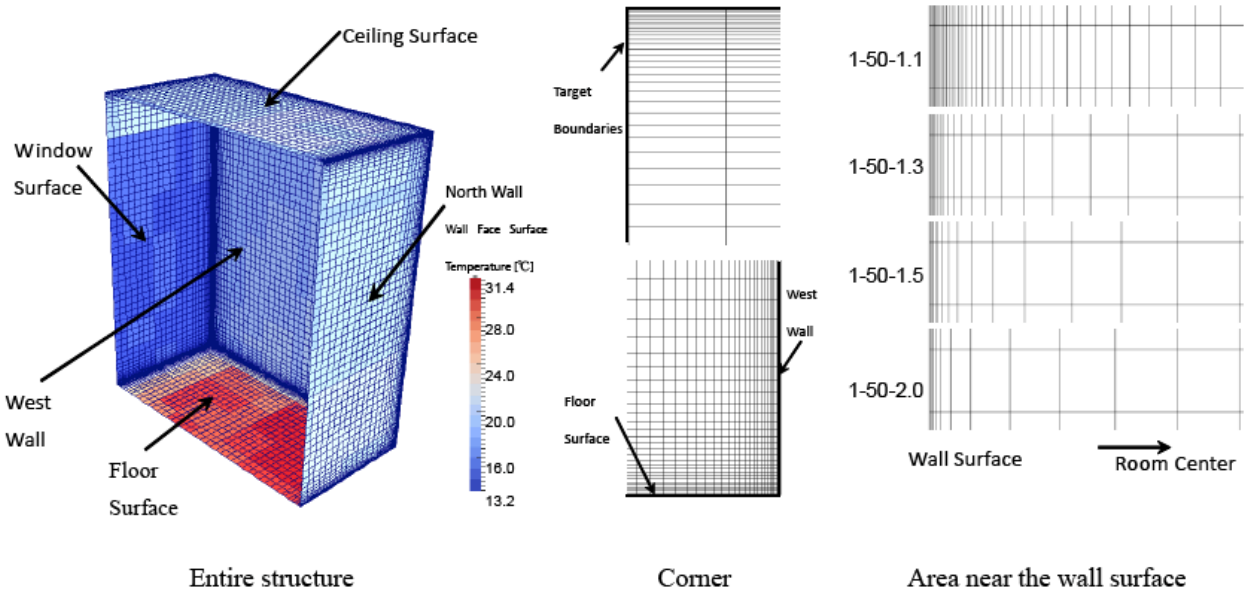

Figure 35: Geometry of the computational mesh.

- Scenario (a): Normal steady-state flows were calculated using a SIMPLE algorithm taken at 32,000 iterations.

- Scenario (b): These steady-state calculations use the same SIMPLE algorithm, and mass properties were averaged at 50,000 iterations to find the computed value.

- Scenario (c): Unsteady-state calculations used the PISO algorithm, and the mass properties were averaged calculated over an adequate time to find the computed value. These results were compared with the actual measurements.

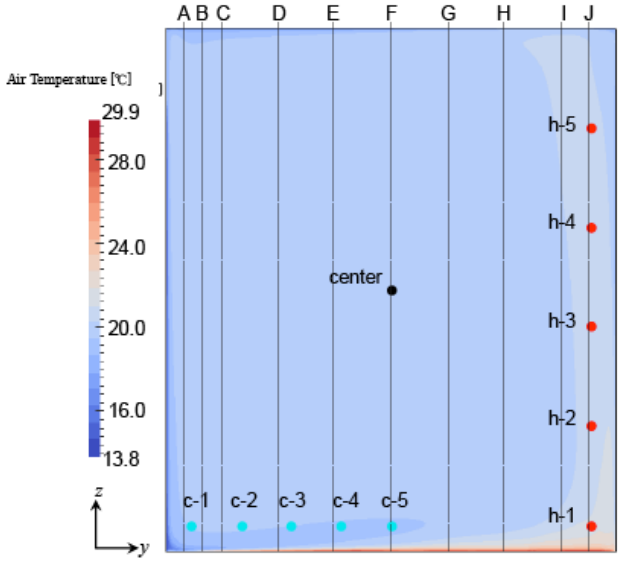

Figure 36: Actual measurement lines and monitoring points.

Figure **37** shows fluctuations in air temperatures computed at the monitoring points (Figure **36**), derived from a steady-state calculation using the SIMPLE algorithm and using the LL turbulence model. Although temperature fluctuations in the center of the room were fairly stable, large fluctuations were produced by the effects of the cold draft at points c-1 to c-5 and by the effects of upward currents emerging from the floor surface at points h-1 to h-5. At point h-1 (near the floor surface), fluctuations of over 4°C are observed and computations may not reach convergence to a single solution even with a large number of iterations. The normalized residual errors in Figure **38** were a little less than 10^{-3}. These errors are small enough to be used in most practical applications; however, it does not appear that these errors can be further reduced.

In Figure **39**, vertical temperature distributions from actual measurements are compared with the results from each of the three scenarios: (a) results at iteration 37,000, (b) results from averaging over 50,000 iterations, and (c) results from time-averaging over 3000 seconds. For lines A–E, which are close to the window panes, the computed results almost match the measurements in all scenarios. However, for lines F–J near the floor surface, some differences appear between the measurements and results from the scenario (a); the largest differences are observed in areas away furthest the window panes, along lines I and J. Even when the SST model was used for the turbulence model, temperature fluctuations did not reach convergence, and differences were observed between the scenario (a) and the measured results near the floor surface. The results from the scenarios (b) and (c) almost matched the results from computation using the LL turbulence model.

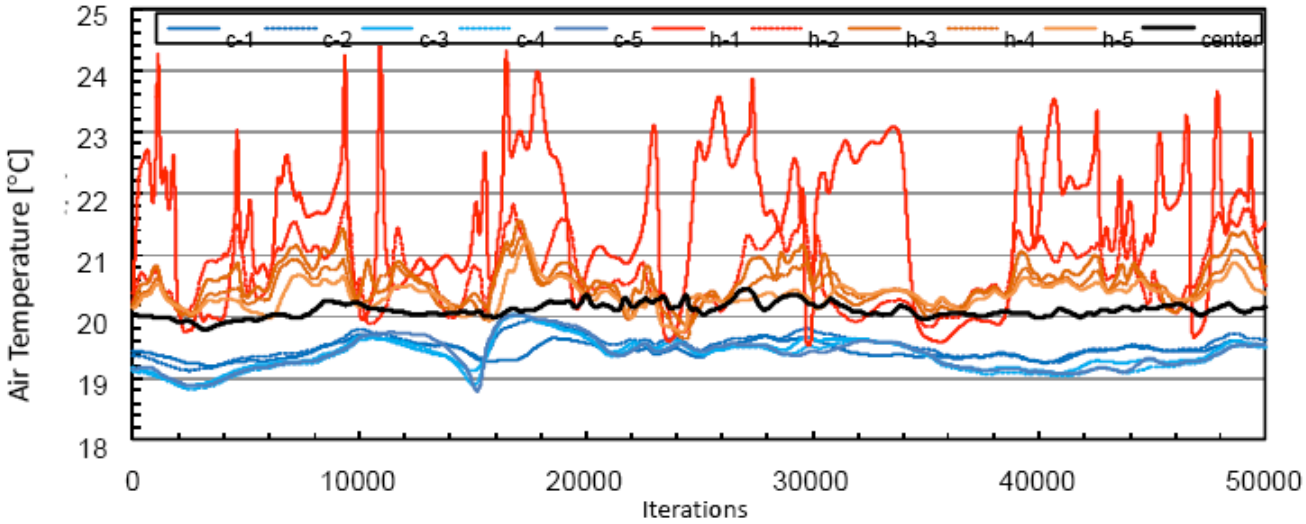

Figure 37: Changes in temperature at monitoring points during steady-state calculations.

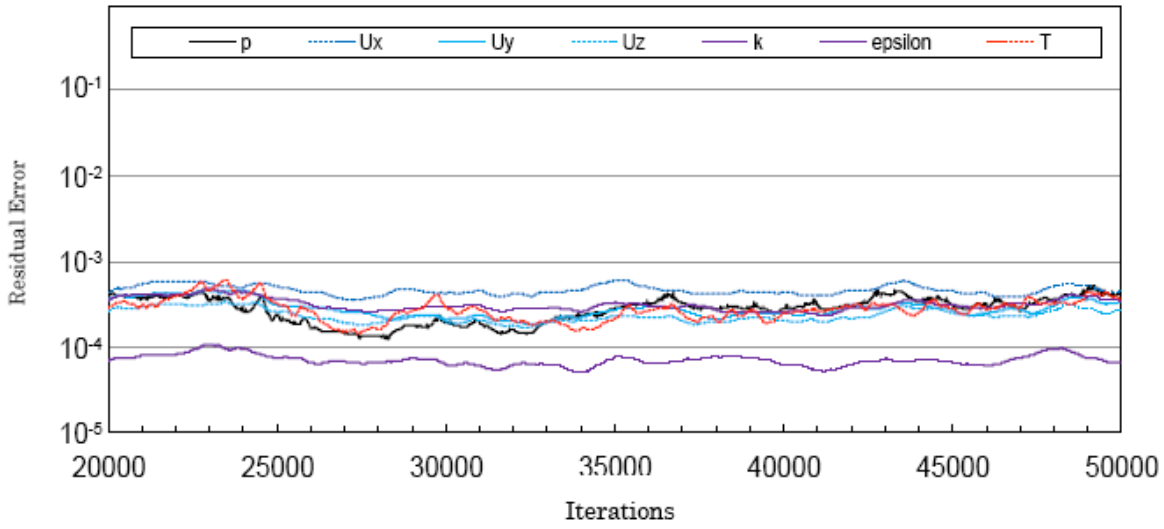

Figure 38: Fluctuations in residuals from each equation during steady-state calculations.

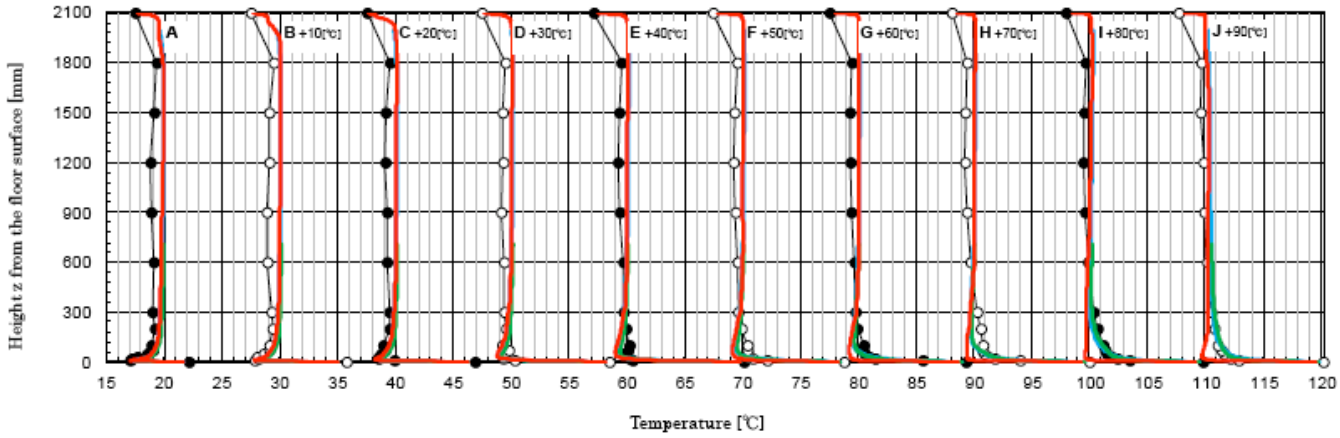

Figure 39: Calculated vertical temperature distributions compared to measured data. Circles: actual measurements. Red lines: Scenario (**a**) at iteration 37,000. Blue lines: Scenario (**b**) averages over 50,000 iterations. Green lines: Scenario (**c**) averages over 3,000 s.

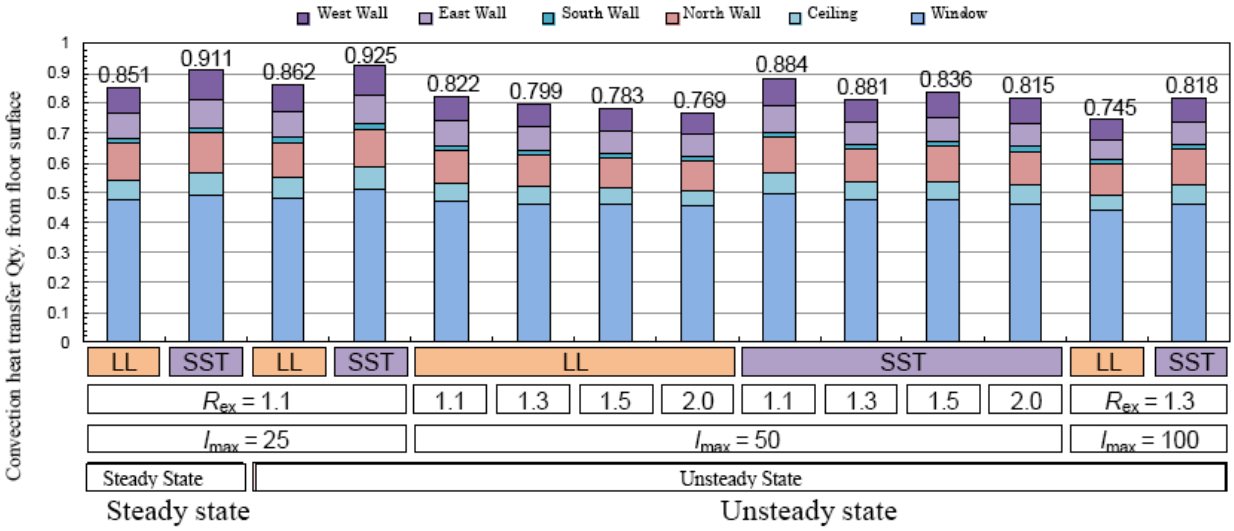

Figure 40: Calculated amounts of convection heat transfer from the floor surface using two turbulence models (LL and SST) and several combinations of mesh parameters. Here, the calculated amounts are relative to the measured amounts of convective heat transfer, which have been set to unity.

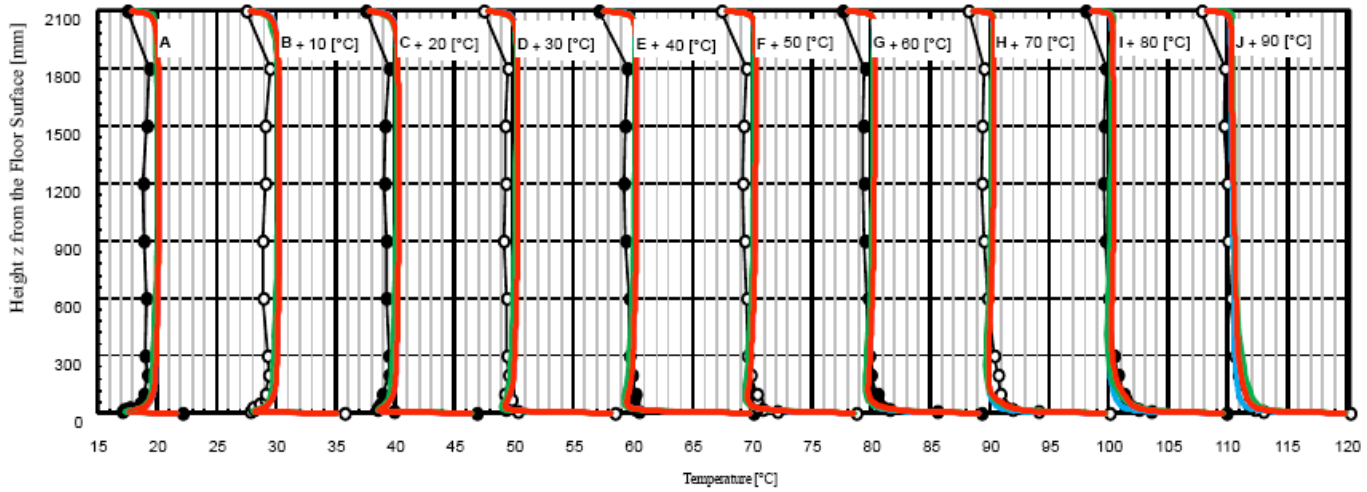

Figure 41: Vertical temperature distributions from unsteady-state calculations compared with the results from actual measurements. Circles: actual measurements. Red lines: 1-25-1.1 mesh. Blue lines: 1-50-1.1 mesh. Green lines: 1-100-1.3 mesh.

Figure **40** compares the convective heat transfer emerging from the floor surface between the models. Similar to the vertical temperature distributions, almost no differences are observed between averaged results taken over iterations in steady-state calculations (scenario (b)) and results from time averaging in unsteady-state calculations (scenario (c)).

Figure **40** Calculated amounts of convection heat transfer from the floor surface using two turbulence models (LL and SST) and several combinations of mesh parameters. Here, the calculated amounts are relative to the measured amounts of convective heat transfer, which have been set to unity.

3.5. Effects of Grid Design

A grid dependence check was also conducted based on unsteady-state calculations using the PISO algorithm. Figure **41** compares vertical temperature distributions using the different mesh parameters defined in Figure **36**. Almost no differences are observed for lines A–G; however, slight differences appear in lines H–J as the maximum cell width increases. Calculated results for l_{max} = 25 mm most closely resemble the actual measurements. We found that even if we changed the enlargement factor R_{ex} using the same l_{max}, the vertical temperature distribution hardly changed. Likewise, we found no critical differences in results when the SST turbulence model was replaced by the LL model.

Figure **40** also shows effects of mesh parameters on the amount of convective heat transfer originating from the floor surface. The convection heat transfer was underestimated in all cases. When the SST turbulence model is combined with mesh 1-25-1.1 (which was closest to the actual measured results), the computed value is lowered by 7.5%. On the other hand, if we combine the LL model with a 1-100-1.3 mesh, the computed heat transfer is more than 25% below that obtained from measured data. On comparing the LL and SST models using the same interstitial spacing, we find that heat transfer amounts from SST are about 5%–10% higher than those from LL, and SST shows fewer differences compared with the actual measurements. At a maximum enlargement rate of R_{ex} = 1.1, both the LL and SST models produce convective heat transfer amounts that most closely resemble values from the actual measurements. As the enlargement rate increases, the amount of convective heat transfer decreases.

3.6. Effects of the Buoyancy Production Term for Dissipation rate ε

We were not able to determine the exact effects that buoyancy has on convection and diffusion of the dissipation rate ε; however, there is also no single decisive method for introducing buoyancy effect into the calculations. In natural-convection fields, the effects of buoyancy production increase; this may also occur in calculation results. Therefore, we evaluated the degree of the effect by studying three models for the coefficient $C_{\varepsilon 3}$. We identify these three models as buoyancy models (d), (e), and (f), which are defined as follows:

(d) $C_{\varepsilon 3} = 1.44$ ($G_k > 0$), $C_{\varepsilon 3} = 0$ ($G_k < 0$)

(e) $C_{\varepsilon 3} = 0$

(f) $C_{\varepsilon 3} = 1.44 \times \tanh|v/u|$

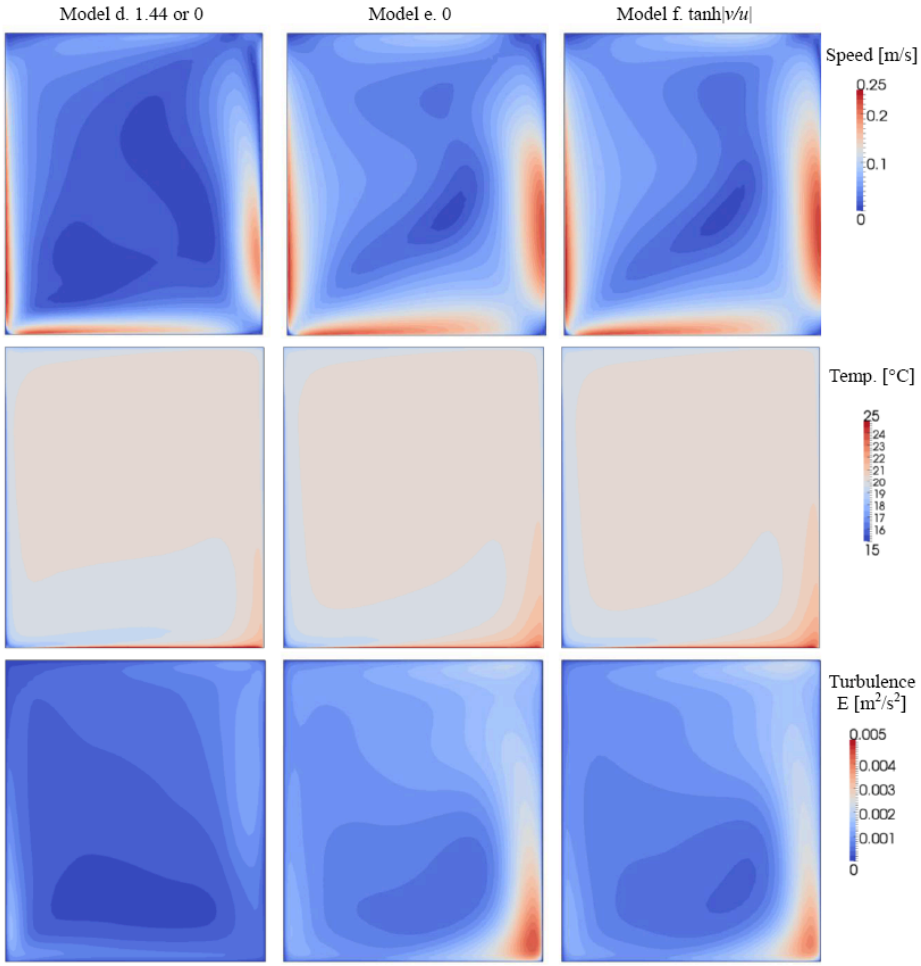

Figure 42: Comparison of midsection distributions for wind speed (top), temperature (middle), and turbulence energy (bottom) from three models for the buoyancy production term for ε. Left vertical panels, Buoyancy Model (d). Middle vertical panels, Buoyancy Model (e). Right vertical panels, Buoyancy Model (f).

Table 9: Amounts of Convective Heat Transfer from Buoyancy Models Buoyancy Model (d), (e), and (f) Compared to Results from Experiment

Actual Measurement Results	d	e	f
93.6 W	73.28 W	87.53 W	86.72 W

Tests of the three buoyancy models were performed using unsteady-state calculations with the PISO algorithm and a 1-50-1.5 mesh. The results for wind speed, temperature, and turbulence kinetic energy distributions are compared in Figure **42**. Buoyancy Model (d) shows small signs of a peak in wind speed next to the wall. In contrast, wind speeds from Buoyancy Models (e) and (f) both spread more toward the middle of the room. For the temperature distributions, outreaches of cold drafts from Buoyancy Models (e) and (f) are much shorter than that from Buoyancy Model (d). There were no differences in the patterns of the turbulence energy distributions among the three models; however, Buoyancy Models (e) and (f) gave higher predictions of turbulence energy compared with Buoyancy Model (d). For the convection heat transfer (Table **9**) Buoyancy Model (d) was about 20% below the actual measurement results. Higher estimations were obtained from Buoyancy Model (e) and (f), which were only a little less than 10% below those found in the actual measurements.

3.7. Summary for Natural Convection in a Room with Floor Heating

Here, we have investigated flow fields created by natural convection from heating panels attached to the floor surface of a room. In addition, we studied how turbulence models, grid partitioning, and computational

algorithms affect computational results. From this, we conclude that it is possible to calculate indoor temperature distributions with accuracies high enough to be useful in practical applications. We assume that CFD programs will be used in actual practice, so we want to clarify the effects that computational parameters have on the results. Our objective is to establish guidelines that identify the minimum computational settings needed to attain a desired level of computational accuracy.

4. CONCLUSIONS

A comprehensive CFD analysis for cross-ventilation flow and flow fields created by natural convection from heating panels attached to the floor surface of a room were performed with OpenFOAM (Code G). In case of cross-ventilation flow, the highest reproducibility of the predicted results compared with the wind tunnel results occurred when the Z_0-type wall function was used as the floor-surface boundary condition and the SST k–ω for the turbulence model. In case of natural convection in a room with floor heating, SST k–ω model showed the closest matching results with experiment.

NOTE

CFD software in conducting benchmark tests were as follows;

(1) Code A: ANSYS/FLUENT®

(2) Code B: ANSYS/CFX®

(3) Code C: CRADLE/STREAM®

(4) Code D: IDAJ/STAR-CD®

(5) Code E: CRADLE/SCRYU Tetra®

(6) Code F: IDAJ/ STAR-CCM+®

(7) Code G: Open FOAM®

(8) Code H: Advanced Knowledge Laboratory/ Flow Designer®

REFERENCES

[1] Ito K, Inthavong K, Kurabuchi T, Ueda T, Endo T, Omori T, *et al*. Benchmark Tests Associated with Applying CFD to Indoor Environmental Problems: Part 1 Benchmark test for isothermal/non-isothermal flow in 2D and 3D room model. Int J Archit Eng Technol 2015; 2(1): 50-71.

[2] Mochida A, Murakami S, Kondo K, Tsuchiya M. Numerical Study on Surface Pressures of Low-Rise Building Using Revised k-ε Model. Seisan-Kenkyu (in Japanese) 1996; 48: 55-59.

[3] Murakami S, Mochida A. Numerical Prediction on the Plume Diffusion Around Building -Study on Buoyant Production Term in ε Equation. Seisan-Kenkyu (in Japanese) 1989; 41: 32-35.

[4] Kurabuchi T, Ooba M, Iwabuchi T, Shimada T. Verification and Stream-tube Analysis of Simulated Result of Airflow of a Cross-ventilated Building for Normal Wind Angle Case: Analysis of airflow of cross-ventilated buildings based on LES and wind tunnel experiment (Part 1). J Archit Plann Environ Eng., Architectural Institute of Japan (in Japanese) 2002; 561: 47-52.

[5] Ooba M, Kurabuchi T, Irie K. Experimental Study on Penetrating Flow and Pressure Loss Through Openings in a Cross-Ventilated Model Building. J Archit Plann Environ Eng., Architectural Institute of Japan (in Japanese) 2002; 552: 21-27.

[6] Architectural Institute of Japan. Guidebook for Practical Applications of CFD to Pedestrian Wind Environment around Buildings. Architectural Institute of Japan (in Japanese) 2007.

[7] Ono H, Sakai K, Kajiya R, Aoki R. Validation of Accuracy of CFD for Natural Convection Flow in Floor Heating Room: Part 1- Temperature Measurement of an Actual-Size Model, in Proceedings of SHASE (The Society of Heating, Air-Conditioning and Sanitary Engineers of Japan), (in Japanese) 2012; 178: 21-27.

[8] Lien FS, *et al*. Low-Reynolds-Number Eddy-Viscosity modeling based on non-linear stress-strain/vorticity relations, Proceedings of.3rd Symposium on Engineering Turbulence Modelling and Measurements 1996; 1-10. http://dx.doi.org/10.1016/B978-0-444-82463-9.50015-0

[9] Wilcox D. Turbulence Modeling for CFD. DCW Industries Inc, 5354 Palm Drive. La Canada, California 91011. 1993.

[10] Menter Fr. Two-equation eddy-viscosity turbulence models for engineering applications. Am Int Aeronaut Asttronaut J 1994; 32: 1598-1605. http://dx.doi.org/10.2514/3.12149

Received on 03-12-2014 Accepted on 18-12-2014 Published on 07-04-2015

DOI: http://dx.doi.org/10.15377/2409-9821.2015.02.01.2